HHS Public Access

Author manuscript

Cell Rep. Author manuscript; available in PMC 2021 December 07.

Published in final edited form as:

Cell Rep. 2021 November 23; 37(8): 110030. doi:10.1016/j.celrep.2021.110030.

The asymmetric *Pitx2* gene regulates gut muscular-lacteal development and protects against fatty liver disease

Shing Hu[1], **Aparna Mahadevan**[1], **Isaac F. Elysee**[1], **Joseph Choi**[1], **Nathan R. Souchet**[1], **Gloria H. Bae**[1], **Alessandra K. Taboada**[1], **Bhargav Sanketi**[1], **Gerald E. Duhamel**[2], **Carolyn S. Sevier**[1], **Ge Tao**[3], **Natasza A. Kurpios**[1,4,*]

[1]Department of Molecular Medicine, College of Veterinary Medicine, Cornell, Ithaca, NY 14853, USA

[2]Department of Biomedical Sciences, College of Veterinary Medicine, Cornell, Ithaca, NY 14853, USA

[3]Department of Regenerative Medicine and Cell Biology, Medical University of South Carolina, Charleston, SC 29425, USA

[4]Lead contact

SUMMARY

Intestinal lacteals are essential lymphatic channels for absorption and transport of dietary lipids and drive the pathogenesis of debilitating metabolic diseases. However, organ-specific mechanisms linking lymphatic dysfunction to disease etiology remain largely unknown. In this study, we uncover an intestinal lymphatic program that is linked to the left-right (LR) asymmetric transcription factor *Pitx2*. We show that deletion of the asymmetric *Pitx2* enhancer *ASE* alters normal lacteal development through the lacteal-associated contractile smooth muscle lineage. *ASE* deletion leads to abnormal muscle morphogenesis induced by oxidative stress, resulting in impaired lacteal extension and defective lymphatic system-dependent lipid transport. Surprisingly, activation of lymphatic system-independent trafficking directs dietary lipids from the gut directly to the liver, causing diet-induced fatty liver disease. Our study reveals the molecular mechanism linking gut lymphatic function to the earliest symmetry-breaking *Pitx2* and highlights the important relationship between intestinal lymphangiogenesis and the gut-liver axis.

Graphical Abstract

*Correspondence: nk378@cornell.edu.

AUTHOR CONTRIBUTIONS

Conceptualization, S.H., A.M., and N.A.K.; methodology, S.H., A.M., C.S.S., and N.A.K.; investigation, S.H., A.M., I.F.E., J.C., N.R.S., G.H.B., A.K.T., B.S., and G.T.; writing – original draft, S.H., writing – review & editing, S.H. and N.A.K.; funding acquisition, S.H. and N.A.K.; supervision, G.E.D., C.S.S., and N.A.K.

DECLARATION OF INTERESTS

The authors declare no competing interests.

SUPPLEMENTAL INFORMATION

Supplemental information can be found online at https://doi.org/10.1016/j.celrep.2021.110030.

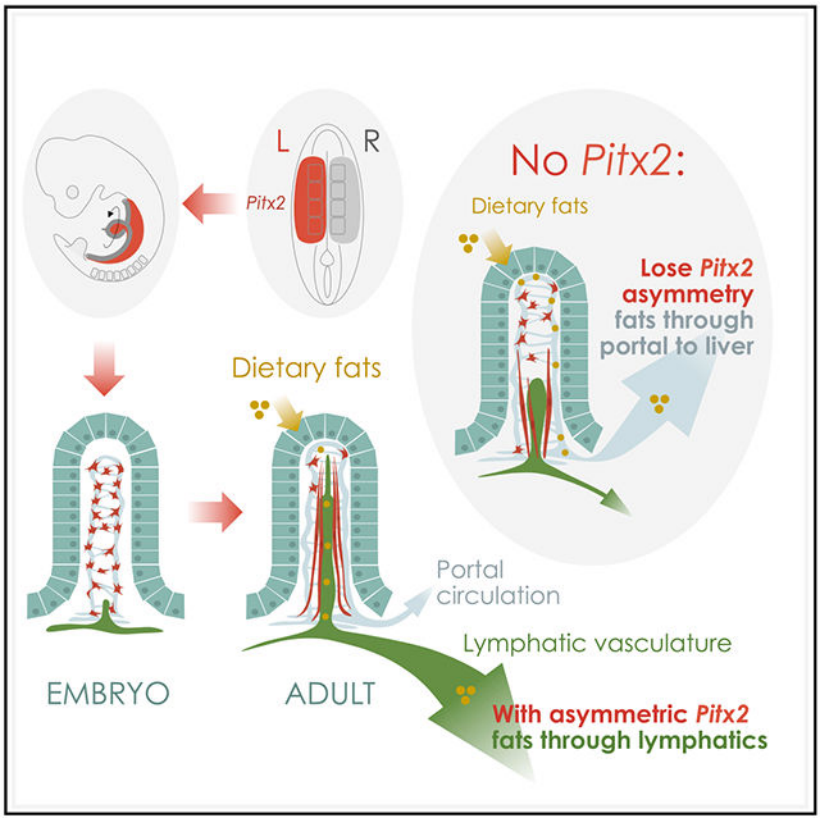

In brief

Lacteals drive dietary lipid absorption, but how they form remains mostly unknown. Hu et al. demonstrate how the *Pitx2* gene directs lacteal development through the adjacent muscle lineage and protects against fatty liver disease. This holds promise for combating intestinal diseases and identifying regulators of alternative fat absorption pathways.

INTRODUCTION

Lymphatic vessels are a crucial component of the cardiovascular system (Alexander et al., 2010a, 2010b; Alitalo, 2011; Alitalo et al., 2005; Bernier-Latmani and Petrova, 2017; Betterman and Harvey, 2016; Cifarelli and Eichmann, 2019; Cueni and Detmar, 2008; Zhang et al., 2018). In the gut, they are essential for absorption and transport of fats and fat-soluble nutrients, a function that distinguishes them from all other lymphatics. However, the developmental programs governing their specialized function remain unknown. Gut lymphangiogenesis depends on prior establishment of arteries within the left side of the dorsal mesentery, the major conduit for blood and lymphatic vessels in the gut (Mahadevan et al., 2014). This process is regulated by the home-odomain transcription factor *Pitx2*, the major player during the evolutionarily conserved left-right (LR) organ asymmetry (Campione et al., 1999; Logan et al., 1998; Ryan et al., 1998; Yoshioka et al., 1998). *Pitx2*$^{-/-}$ mouse embryos have gut arterial patterning defects and fail to initiate gut but

not dermal lymphangiogenesis, suggesting an organ-specific lymphatic role for *Pitx2* (Mahadevan et al., 2014).

The *Pitx2* gene includes three distinct isoforms: *Pitx2a*, *Pitx2b*, and *Pitx2c* (Figures 1A-1C). The *Pitx2ab* splice variants share the same promoter and are expressed bilaterally, whereas *Pitx2c* is transcribed from a separate promoter and is expressed asymmetrically (Liu et al., 2001; Schweickert et al., 2000; Shiratori et al., 2001, 2006). Left-specific *Pitx2c* expression is conferred by the conserved enhancer *ASE* (Shiratori et al., 2001, 2006). $Pitx2^{ASE/ASE}$ mice fail to manifest most of the left-sided *Pitx2c* expression and exhibit laterality defects similar to those observed in mice lacking *Pitx2c* (Liu et al., 2002). Unlike $Pitx2^{-/-}$ embryos lacking all isoforms ($Pitx2^{HD/HD}$) (Lu et al., 1999), most $Pitx2^{ASE/ASE}$ embryos survive to birth, and a few can reach weaning, allowing analyses of gut lymphatic function in the absence of *ASE* (Figures 1B and 1C).

We first focused on lacteals, the absorptive lymphatic capillaries responsible for dietary fat uptake (Cifarelli and Eichmann, 2019; Miller et al., 2010). Fatty nutrients use lacteals as their major transport route, where chylomicron-packed lipids drain into larger mesenteric collectors and, ultimately, to the systemic blood circulation (Bernier-Latmani and Petrova, 2017; Dixon, 2010; Ko et al., 2020; Wang et al., 2013). In contrast, non-lipid nutrients enter the portal (venous) circulation for delivery to the liver (Bernier-Latmani and Petrova, 2017; Dixon, 2010; Ko et al., 2020; Wang et al., 2013). Lacteals form around embryonic day 17.5 (E17.5) and are functionally ready to absorb lipids from milk at birth (Kim et al., 2007). Signaling via lymphangiogenic vascular endothelial growth factor C (VEGF-C), its receptor VEGFR-3, and its co-receptor neuropilin 2 (NRP2) plays a key role in driving postnatal lacteal sprouting and growth (Tammela et al., 2008; Xu et al., 2010). Although most adult lymphatics are quiescent, lacteals undergo filopodium-mediated regeneration (Bernier-Latmani et al., 2015). Although most lymphatic capillaries lack smooth muscle coverage, lacteals are surrounded by contractile axial smooth muscle cells (SMCs) (Hosoyamada and Sakai, 2007), which secrete VEGF-C (Nurmi et al., 2015) and facilitate lipid transport by squeezing the lacteal (Choe et al., 2015).

Here we show that *Pitx2* is required for development and function of lacteals through a non-cell-autonomous pathway that involves lacteal-associated axial SMCs. *ASE* deletion results in abnormal axial SMC morphogenesis caused by oxidative stress, leading to impaired lacteal extension and defective lymphatic system-dependent lipid transport. Strikingly, *ASE* deletion leads to excessive portal entry of dietary lipids and severe hepatic lipidosis in pups. Our study reveals a molecular mechanism linking gut lymphatic function to *Pitx2* and highlights the important relationship between the intestinal lymphatic vasculature and gut-liver axis. We show that *Pitx2* continues to orchestrate postnatal intestinal function beyond its well-established roles in early LR asymmetry.

RESULTS

Loss of the LR Pitx2 asymmetric enhancer (ASE) results in growth retardation and early postnatal lethality

Although most *Pitx2*$^{ASE/ASE}$ mice die within hours after birth (C57BL/6 × 129 mixed background), some *ASE* newborns on the FVB background remain viable for ~10 days (21.6%; Figure 1C; Figure S1) or longer (4.7% at weaning; Figure 1C), allowing analyses of gut lymphatic development and function in the absence of *ASE*. To evaluate intestinal lymphatic function in dietary lipid transport, we first compared post-feeding weight gain between wild-type (WT), *Pitx2*$^{ASE/+}$, and *Pitx2*$^{ASE/ASE}$ neonates. Despite their comparable body weights at birth, *Pitx2*$^{ASE/ASE}$ had severely retarded growth at 24–48 h and at postnatal day 9 (P9) (Figure 1D; Figure S1). This was independent of variable food ingestion; ample milk was seen in all neonatal stomachs analyzed, regardless of genotype (Figure 1D). We hence hypothesize that the failure of proper weight gain seen in *Pitx2*$^{ASE/ASE}$ mice was due to malabsorption caused by compromised lymphatic transport function.

ASE is required for lacteal extension and formation of lacteal filopodia

Intestinal lipid transport is driven by lacteals (Figure S2A); hence, we characterized lacteal development in *Pitx2*$^{ASE/ASE}$ mice, in which they are detectable as early as E17.5, using the lymphatic endothelial cell marker Lyve-1 (Kim et al., 2007; Figure S2A). We compared embryonic and postnatal lacteal development between WT and *Pitx2*$^{ASE/ASE}$ mice using IF on gut slices (Figure S2B). First we observed a significant reduction in the number of Lyve-1^{+} lacteals in *Pitx2*$^{ASE/ASE}$ embryos at E18.5 (Figure S2C) and again at P9 (Figure S2C; Figures 3B and 3D, asterisks) despite unaffected villus length (Figure S2C). Lymphatic endothelial cells (LECs) at the tip of the lacteals extend long filopodia in WT neonatal intestines, consistent with active sprouting and migration (P1.5; Figure 2A, arrows; Adams and Alitalo, 2007). In the WT, ~73% of lacteals harbor at least one filopodium at P1.5 (Figure 2A; 72.90% ± 2.760%, n = 16), in agreement with prior studies in adulthood (Bernier-Latmani et al., 2015). In contrast, most *Pitx2*$^{ASE/ASE}$ lacteals are missing filopodia at P1.5 (Figure 2A, arrowheads; 41.28% ± 3.545%, n = 10, p = 0.0001). Similar results were obtained following isoform-specific deletion of *Pitx2c* (Figure 2B; WT: 81.38% ± 4.660%, n = 3; *Pitx2c*$^{-/-}$, 41.13% ± 5.604%, n = 4; p = 0.0034). Filopodium formation remained suppressed during later stages of development (P9), a phenotype that was exacerbated over time (Figure 2C; WT, 49.66% ± 4.200%, n = 8; *Pitx2*$^{ASE/ASE}$, 8.543% ± 2.610%, n = 3; p = 0.0003).

Consistent with filopodium defects, *Pitx2*$^{ASE/ASE}$ lacteals were significantly shorter than those of WT littermates at P1.5 (Figure 2A; WT: 176.1 ± 6.401 μm, n = 17; *Pitx2*$^{ASE/ASE}$: 143.7 ± 6.392 μm, n = 10; p = 0.0026) and again at P9 (Figure 2C; WT: 222.7 ± 8.252 μm, n = 8; *Pitx2*$^{ASE/ASE}$: 144.6 ± 9.518 μm, n = 3; p = 0.0005). Although WT lacteals elongated by ~50 μm from P1.5 to P9 (Figures 2A and 2C; P1.5: 176.1 ± 6.401 μm, n = 17; P9: 222.7 ± 8.252 μm, n = 8), such lacteal extension was halted in *Pitx2*$^{ASE/ASE}$ mice despite normal villus length (Figures 2A and 2C; P1.5: 143.7 ± 6.392 μm, n = 10; P9: 144.6 ± 9.518 μm, n = 3). *ASE* is required for proper lacteal extension and lacteal filopodium formation.

Pitx2 daughter cells populate lacteal-associated smooth muscle

To determine whether *Pitx2* acts autonomously in LECs or in a non-cell-autonomous manner, we performed *Pitx2*^{Cre} (knockin) lineage tracing to fate map *Pitx2* descendants (Figures S3A-S3A"). *Pitx2*^{Cre} is a null *Pitx2* allele that drives Cre activity in cells that have expressed any *Pitx2* isoform throughout embryonic development (Liu et al., 2002; Figure S3A). To follow *Pitx2* daughter cells, we crossed *Pitx2*^{cre} heterozygotes with *Rosa26* (*R26R-tdTomato*) reporter mice (Figure S3A).

TdTomato-marked *Pitx2* daughters were detected in the intestine, consistent with the described role of *Pitx2* during midgut development (Figure S3A'). *Pitx2* daughters did not populate CD31-positive blood endothelial cells (BECs) or Lyve1^{+} LECs at any time point analyzed (E14.5, E16.5, E18.5, P1.5, P9, and 6 months; n = 19) (Figure S3A"). Instead, we found *Pitx2* daughter cells among the α-smooth muscle actin (αSMA)-positive SMCs of the intestine, including villus-axial SMCs that are closely associated with lacteals (Bernier-Latmani and Petrova, 2016; Hosoyamada and Sakai, 2007; Figures 3A′-3A‴, white arrowheads, and 3B, WT). We confirmed this observation using *ASE*-specific lineage tracing with *Rosa26* (*R26R-EYFP*) reporter mice, where the activity of Cre is driven by an ~18-kb genomic fragment containing *ASE* and the *Pitx2c* promoter (Shiratori et al., 2014; Figure 3A⁗, white arrowheads).

In addition to axial SMCs, we found a discrete fraction of TdTomato-marked *Pitx2* (Figure 3A′, white arrows) and YFP-marked *ASE* (Figure 3A⁗, white arrows) daughter cells morphologically different from axial SMCs and near, but distinct from, the CD31^{+} blood capillary plexus of the villous *lamina propria* (Figure 3A″, white arrows). Based on their location and morphology, these cells may lie upstream in the lineage compared with the more differentiated axial SMCs and may be involved in muscular regeneration or expansion at later stages (Figure 3A‴, white arrows, 6 months). *Pitx2* regulates lacteal development through a non-cell-autonomous pathway and may contribute to SMC patterning of the intestinal *lamina propria*.

Loss of ASE impairs lacteal-associated axial smooth muscle development

Contraction of axial SMCs drives lipid transport in adjacent lacteals (Choe et al., 2015), whereas a subset of axial SMCs secretes VEGF-C (Nurmi et al., 2015). Loss of VEGF-C-driven VEGFR-3 activation leads to arrested lacteal growth (Nurmi et al., 2015). We hence hypothesized that *Pitx2* is indirectly required for lacteal morphogenesis via SMC patterning. Under histological examination of P26 weanlings, robust villus axial SMCs were seen in the WT, but limited SMCs were observed in *Pitx2*$^{ASE/ASE}$ mice (Figure S3B, red arrowheads). To characterize the muscular-lacteal complex at high resolution, we examined WT and *Pitx2*$^{ASE/ASE}$ gut slices using confocal microscopy with αSMA (smooth muscle) and Lyve-1 (lacteal) IF. In WT pups at P9, αSMA^{+} cells were closely intertwined with Lyve-1^{+} lacteals. This striking pattern of "closed" muscle bundle morphology suggests active muscular contractions squeezing the lacteal (Figures 3B and 3E). In contrast, age-matched *Pitx2*$^{ASE/ASE}$ mice displayed a wide spectrum of muscle-lacteal abnormalities, including misaligned axial SMCs with absent lacteals, reduced axial SMC numbers, loss of direct SMC-LEC contact, and an "open" bundle conformation leaving spaces between

individual muscle bundles and lacteals (Figures 3B and 3E). We quantified a significant increase in open axial smooth muscle bundles within *Pitx2*$^{ASE/ASE}$ villi compared with control mice (Figures 3B and 3C; WT: 33.51% ± 3.950%, n = 6; *Pitx2*$^{ASE/ASE}$: 76.12% ± 7.775%, n = 3; p = 0.0009). Using villus sections, we confirmed that axial SMCs and lacteals fail to align in *Pitx2*$^{ASE/ASE}$ mice (Figures 3D and 3E). This supports the hypothesis that *ASE* regulates villus axial SMC morphogenesis.

Lacteal-associated axial SMCs arise by ASE-dependent remodeling

Villus-axial SMCs were first identified in 1909 (Trautman, 1909) and were considered vital to provide structural tension against interstitial pressure while driving villous rhythmical contraction in close relationship with the adjacent fibroblasts (Güldner et al., 1972; Hosoyamada and Sakai, 2007). More recent *in vivo* imaging revealed that villus SMCs promote lateral villus contractions dependent on the autonomic nervous system and facilitate lipid transport by squeezing the lacteal (Choe et al., 2015). Despite this crucial interplay between axial SMCs and lacteal function, the origins and patterning mechanisms of axial SMCs remain unexplored.

We investigated muscle formation alongside lacteals in WT mice from E16.5–P9 (Figure 4A; Figure S4A). Cells with low levels of αSMA (αSMA^{+}) were first detected in the villus at E16.5, before emergence of lacteals (Figure S4A). αSMA^{+} cells within the villus appeared star-shaped with multiple protrusions (Figure 4A, inset, “star cells”) and aligned closely with the CD31^{+} blood vascular plexus (Figure S4A). Interestingly, αSMA^{+} star cells were reminiscent of TdTomato-marked *Pitx2* and YFP-marked *ASE* daughters (Figures 3A’ and 3A″″, white arrows). Coincident with the appearance of lacteals at E18.5, αSMA^{+} cells underwent a robust transformation to form elongated, spindle-like cell types with strong immunoreactivity for αSMA (αSMA^{++}) that closely associate with lacteals (Figure 4A, graph). At P1.5, the number of spindle-like αSMA^{++} cells became predominant at the expense of αSMA^{+} star cells (Figure 4A, graph). At P9, all αSMA^{++} spindle cells were located adjacent to the lacteal, extending radially from the submucosa to the filopodium at the tip of the lacteal, whereas very few αSMA^{+} star cells were detected at this time (Figure 4A; Figure S4D).

αSMA^{+} star cells were proliferative (Figure S4B; Figure 4B ~10%) compared with αSMA^{++} spindle-like axial SMCs (Figure S4B; Figure 4B). This agrees with previous observations that only round muscular progenitors (but not mature spindle muscles) are proliferative (Owens, 1995; Owens et al., 2004). αSMA^{++} spindle cells expressed high levels of myosin heavy chain 11 (Myh11), resembling more differentiated muscle cells (Gomez et al., 2015; P9, Figure S4D). In contrast, αSMA^{+} star cells showed very weak Myh11 immunoreactivity (P9; Figure S4D, white arrows). These observations suggest that villus-axial smooth muscle development is commensurate with formation of lacteals and proceeds by a robust spatiotemporal remodeling program where αSMA^{+} precursor star cells proliferate and assemble to create and shape the mature axial SMCs network of the lacteal (Figure 4E). Axial SMCs were largely juxta-vascular, and this was especially evident for SMCs at the lacteal filopodia (Figure S4C), highlighting an important reciprocal interaction with the adjacent lymphatic endothelium.

Next we examined villus-axial SMCs dynamics in the absence of *ASE*. As in WT villi, we first detected αSMA^{+} star cells in the *Pitx2*$^{ASE/ASE}$ at E16.5, with no differences in the proportion of villi containing αSMA^{+} star cells among all genotypes tested (data not shown). However, 2 days later, at E18.5, we found fewer αSMA^{++} spindle-like axial SMCs in *Pitx2*$^{ASE/ASE}$ mice compared with WT littermates (Figure 4D; WT: 62.98% ± 7.52%, n = 6; *Pitx2*$^{ASE/ASE}$: 36.93% ± 4.41%, n = 6; p = 0.0136). In contrast to WT neonates, a significant number of αSMA^{+} star cells remained in the *lamina propria* of *Pitx2*$^{ASE/ASE}$ at P1.5 (Figures 4C and 4D; WT: 12.25% ± 4.917%, n = 6; *Pitx2*$^{ASE/ASE}$: 42.42% ± 3.510%, n = 5; p = 0.0010). These star cell-retained *Pitx2*$^{ASE/ASE}$ villi (Figure 4C, white arrows) had less prominent muscular bundles surrounding the lacteals (Figure 4C, white arrowheads).

TUNEL staining of WT and *Pitx2*$^{ASE/ASE}$ at P9 revealed no difference in cell death of villous SMCs (Figure S4E). Under histopathological analyses, apoptotic or necrotic cells were not seen in E18.5, P1.5, and P9 *Pitx2*$^{ASE/ASE}$ villi, whereas villous SMC proliferation was similarly unaffected in *Pitx2*$^{ASE/ASE}$ mice at E18.5 (data not shown). These observations suggest that neither cell death nor cell cycle arrest at the stages examined contribute to the *ASE*-dependent axial SMC phenotypes. Instead, we propose that *ASE* functions in villous-axial SMC morphogenesis during their fetal to neonatal transition (Figure 4E).

ASE deletion leads to redox imbalance in intestinal smooth muscle

To explore the cause of muscular-lacteal impairment in *Pitx2*$^{ASE/ASE}$ intestines, whole-intestine transcriptomics (RNA sequencing [RNA-seq]) of WT and *Pitx2*$^{ASE/ASE}$ tissue at P1.5 was performed. Notably, ~20% of genes differentially expressed between WT and *Pitx2*$^{ASE/ASE}$ intestines corresponded to reactive oxygen species (ROS) production, antioxidant scavenging genes, and redox-sensitive signaling pathways (Figure 5A). Unsupervised gene set enrichment analysis (GSEA) demonstrated an enriched ROS pathway in *Pitx2*$^{ASE/ASE}$ intestine (normalized enrichment score = 1.43, nominal p = 0.03, false discovery rate [FDR] q = 0.03) (Subramanian et al., 2005; Figure S5A). Among potential targets were genes that protect the cell from oxidative stress, such as the glutamate-cysteine ligase (*Gclc*), the first rate-limiting enzyme of glutathione synthesis (Fedorova et al., 2014; Lu, 2013; Wang et al., 2014). Interestingly, half of the ROS-related differentially expressed genes are bound by Pitx2 *in vivo* (Wang et al., 2014), including the noncoding region of *Gclc* (Figure S5B). These data raised the possibility that *Pitx2c* may directly regulate the redox balance in intestinal smooth muscle.

To investigate whether *ASE* deletion leads to a redox imbalance in the intestine, we spectrophotometrically detected and quantified protein carbonylation in WT, Pitx2$^{ASE/+}$, and Pitx2$^{ASE/ASE}$ neonatal intestines at P1.5. Carbonyl groups (Figure 5B) are irreversible products of ROS-mediated protein oxidation and a general biomarker for oxidative injury (Chevion et al., 2000; Dalle-Donne et al., 2003b; Fedorova et al., 2014). We observed that Pitx2$^{ASE/ASE}$ intestines harbor 2.5 times more protein carbonyl content compared with their WT or Pitx2$^{ASE/+}$ littermates (Figure 5B'; WT/Het: 2.760 ± 0.3194 nmol/mg, n = 7; *Pitx2*$^{ASE/ASE}$: 6.833 ± 0.4567 nmol/mg, n = 3; p = 0.0001), demonstrating that *ASE* loss causes oxidative damage. We also assessed protein carbonyl by electrophoresis,

after labeling carbonyl groups in protein extracts from WT, *Pitx2*$^{ASE/+}$, and *Pitx2*$^{ASE/ASE}$ intestines at P1.5 with biotin-hydrazine (biotin-HZ). Proteins were SDS-PAGE-separated and probed with streptavidin-conjugated horseradish peroxidase (SA-HRP). Consistent with the spectroscopic measurements, a higher total level of carbonylated proteins (overall darker lane signal) was observed in the Pitx2$^{ASE/ASE}$ intestine lysate relative to controls (Figure 5C).

Interestingly, a well-defined carbonylated protein band of ~42 kDa was enriched in *Pitx2*$^{ASE/ASE}$ intestinal extracts versus controls (Figure 5C). This band is consistent in size with monomeric actin. Probing the same lysates for αSMA showed that actin levels were similar among all genotypes (Figure 5C), suggesting the possibility that levels of oxidized actin were enriched in *Pitx2*$^{ASE/ASE}$ intestines.

The dynamic actin cytoskeleton is susceptible to oxidation, which regulates cell behavior and contractility pathways (Xu et al., 2017). Oxidized actin is linked to decreased actin monomer (G-actin) assembly and actin filament (F-actin) stability (Wilson and González-Billault, 2015). Oxidation of select cysteine and methionine residues in actin causes structural changes, monomer aggregation, decreased actin polymerization and stability, and defective cell contractility (Dalle-Donne et al., 2002, 2003a; Hung et al., 2011, 2013). Actin carbonylation is associated with even higher oxidant levels than those associated with modification of critical cysteine and methionine residues, and an accumulation of carbonylated actin has been proposed to indicate severe oxidative stress and functional impairment (Dalle-Donne et al., 2001). Interestingly, we noted discontinuous patterns of αSMA arrangement in the axial SMCs of the more severely affected *Pitx2*$^{ASE/ASE}$ mice, reminiscent of the severed F-actin filaments seen under oxidative stress (Figure S5C). These data led us to hypothesize that *ASE* deletion impaired villus-axial smooth muscle morphogenesis because of abnormal accumulation of ROS in the differentiating smooth muscle.

To test this, we directly assessed the oxidation status of SMA in WT and *Pitx2*$^{ASE/ASE}$ neonatal intestines (Figures 5D and 5E). Streptavidin enrichment of biotin-labeled carbonylated proteins confirmed that actin was carbonylated and that *Pitx2*$^{ASE/ASE}$ yielded the highest amount of carbonylated αSMA (Figure 5D). Immunoisolation of αSMA from biotin-HZ-labeled lysates similarly confirmed an increased level of carbonylated αSMA in *Pitx2*$^{ASE/ASE}$ intestine in comparison with WT or *Pitx2*$^{ASE/+}$ littermates (Figure 5E). These results demonstrate that loss of *ASE* induced irreversible oxidative damage in αSMA^{+} cells of the neonatal intestine. Our data suggest that elevated levels of oxidative stress caused muscular-lacteal impairment in *Pitx2*$^{ASE/ASE}$ intestines, pointing to a crucial role of *Pitx2* in the control of ROS during early smooth muscle development.

ASE is required for the normal route of dietary lipid transport

The lymphatic vasculature is the major route through which long-chain fatty acids are absorbed into the body (Zhou et al., 2020). In contrast, non-fatty nutrients and shorter-chain fatty acids are able to directly enter the hepatic portal circulation for processing within the liver (Zhou et al., 2020). This lymphatic system-independent portal transport is insignificant compared with the lymphatic route, except under pathological conditions leading to hepatic

lipid accumulation (Anwar et al., 2007; Cabré et al., 2005; Courtney and Warner, 2017; Ee et al., 2000; Fujimoto et al., 1991; Hussain, 2014; Kurtel et al., 1991; McDonald et al., 1980; Onufer et al., 2019; Young et al., 1995). To assess whether *ASE* deletion impaired dietary lipid transport, we orally administered fluorescent BODIPY C16, a fluorescent long-chain fatty acid tracer, to WT and *Pitx2*$^{ASE/ASE}$ neonates to follow lipid trafficking (Figure 6A; Dixon et al., 2009). As expected, BODIPY C16 entered the lumen of the intestine and mesenteric collecting vessels after oral administration (Figure 6A), with very little staining of the hepatic portal circulation in WT pups (Figure 6B). Strikingly, long-chain BODIPY C16 accumulation was found in the hepatic portal vein and liver parenchyma of *Pitx2*$^{ASE/ASE}$ pups (Figure 6B; liver, liver section, and hepatic portal vein), confirming abnormal lipid transport in the absence of *ASE*. Notably, BODIPY C16 remained detectable in the mesenteric collectors of *Pitx2*$^{ASE/ASE}$ pups, implying a partial rather than complete shift in lipid transport in the absence of *ASE* (Figure S6). Thus, *ASE* deletion impairs normal long-chain fatty acid lymphatic trafficking, resulting in direct lipid entry into the hepatic portal circulation (Figure 6C).

Pitx2$^{ASE/ASE}$ mice develop diet-induced fatty liver disease

Aberrant dietary lipid transport by the hepatic portal vein can accumulate lipid within hepatocytes, resulting in hepatic lipidosis. We compared liver lipid content in prenatal and postnatal WT and *Pitx2*$^{ASE/ASE}$ mice using oil red O, a fat-soluble dye that stains neutral triglycerides and lipids (Mehlem et al., 2013; Figure 7A). Consistent with our BODIPY C16 data, increased oil red O staining in postnatal but not prenatal (unfed) Pitx2$^{ASE/ASE}$ liver suggested an etiology related to post-partum nursing. Excessive hepatic lipid accumulation was observed in 100% of *Pitx2*$^{ASE/ASE}$ pups at P1.5 (Figure 7A). This was confirmed by ultrastructural examination (Figure S7A) and quantitative triglyceride analysis (Figure S7C).

At P9–P11, oil red O staining was even more robust (Figure 7A). Histopathology analysis at P9 revealed a 92% incident of hepatic steatosis in Pitx2$^{ASE/ASE}$ mice (Figure S7B) with variable parenchymal extinction and multifocal subcapsular mineralization (Figure 7B). Importantly, no significant changes in hepatic structure, mitochondrial morphology, or extramedullary hematopoiesis were observed between Pitx2$^{ASE/ASE}$ and WT littermates (data not shown), ruling out primary liver impairment.

Although the lipid content of murine maternal milk is ~17%–30% (Görs et al., 2009), the lipid content in standard mouse chow diet is 6- to 10-fold lower (~3%). Hepatic steatosis in *Pitx2*$^{ASE/ASE}$ suckling pups gradually resolved when weaned (P21) and transitioned to a dry pellet diet (Figure 7B). Severe hepatic lipidosis in *Pitx2*$^{ASE/ASE}$ mice was seen in only 50% of pups at P21 and was reduced further to 25% at P26 and 0% after P30 (Figure S7B). Importantly, the intestinal lesions caused by *ASE* deletion did not resolve with age or weaning/change of diet. These lesions included lacteal filopodium defects (Figure 7C; WT: 28.81% ± 7.915%, n = 5; Pitx2$^{ASE/ASE}$: 5.833% ± 3.967%, n = 4; p = 0.0012), open axial smooth muscle (Figure 7C; WT: 13.08% ± 2.637%, n = 5; Pitx2$^{ASE/ASE}$: 73.85% ± 9.599%, n = 4; p = 0.0003), and severe axial smooth muscle hypoplasia (Figure S3B). This is a strong indication that mature mice remain susceptible to lipid accumulation, depending on their diet. These data suggest that a high-fat diet (in this case maternal milk) drives fatty liver

in Pitx2$^{ASE/ASE}$ mice, whereas *Pitx2c* protects against such pathogenesis in the WT (Figure S9).

DISCUSSION

Pitx2 in intestinal smooth muscle development

LR asymmetry is fundamental to the vertebrate body plan, errors in which cause important human birth defects. The intestine begins as a symmetrical midline tube but later rotates and loops in a conserved pattern to pack into the body cavity. The first critical leftward midgut rotation is driven by molecular and morphologic asymmetries within the left and right sides of the dorsal mesentery. These events are orchestrated by *Pitx2* expressed in all cells of the left dorsal mesentery (Davis et al., 2008). Although *Pitx2*$^{ASE/ASE}$ mice exhibit duodenal (foregut) positioning defects (Shiratori et al., 2006), no midgut rotation, strangulation, or vascular obstruction are apparent in these mice (Shiratori et al., 2006; Figures S6 and S8A). Further analysis of blood vascular organization (Figure S8B), histopathology (Figure S8C), and staining for the hypoxia marker HIF-1α (data not shown) support that the lacteal-muscle defects caused by loss of *ASE* are not caused indirectly by confounding physiological factors or intestinal topology.

The dorsal mesentery is also the major source of gut smooth muscle progenitors (Wilm et al., 2005; Winters et al., 2014). *Pitx2* descendants populate multiple intestinal smooth muscle layers, including the lacteal-associated axial SMCs that drive lacteal contraction and postnatal lipid transport (Choe et al., 2015). Interestingly, not all axial SMCs are descendants of *Pitx2* (Figures 3A” and A”’), suggesting heterogeneity among axial SMCs and hinting at an additional progenitor source. Although *Pitx2* is the primary determinant in the left dorsal mesentery, the transcription factor *Tbx18* is enriched exclusively on the right side (Davis et al., 2008; Welsh et al., 2013). In the kidney, *Tbx18*-derived stromal progenitors give rise to vascular SMCs, where stromal cell differentiation requires *Tbx18* to form the renal vasculature (Airik et al., 2006; Xu et al., 2014a). The right-sided origin *Tbx18* lineage may provide an additional source of axial SMCs that is functionally distinct from the *Pitx2* lineage. Similar heterogeneity has been demonstrated recently among villous fibroblasts, highlighting the *lamina propria* milieu in the overall integrity and function of intestinal lymphatics (Hong et al., 2020).

Pitx2 daughters were also found near the villous blood capillary plexus, suggesting that they are blood capillary-associated mesenchymal precursors to axial SMCs (Figures 3A’ and A””). A *Pitx2* daughter subpopulation was also present in the circular and longitudinal smooth muscle of the *muscularis externa* (data not shown), suggesting that *Pitx2* may regulate gut motility and lymph propulsion through peristalsis. Indeed, *Pitx2* modulates the expression of contractile proteins in skeletal muscle, including myosin heavy chains (MyHCs) and troponin I and T (Zhou et al., 2011). During myogenesis, *Pitx2* is downstream of Pax3/7 and upstream of Myf5, Myf6, and MyoD (L’honoré et al., 2010; Lagha et al., 2010). Mutations of *Pitx1*, *Pitx2*, and *Pitx3* result in human developmental defects involving muscle disorders, such as facioscapulohumeral muscular dystrophy (Dixit et al., 2007), Axenfeld-Rieger syndrome (Semina et al., 1996), and anterior segment mesenchymal dysgenesis (Semina et al., 1998), respectively. Current literature on *Pitx2* in control of

myogenesis concerns skeletal muscle (from paraxial mesoderm). Here we provide insight into *Pitx2* function in visceral smooth muscle (splanchnic mesoderm). We speculate that Pitx transcription factors regulate muscle biogenesis and function at their distinct spatiotemporal sites of expression.

Pitx2-dependent formation of the lacteal-associated axial SMC complex

Recent studies have revealed the detailed developmental program of the *muscularis externa* (Huycke et al., 2019), but the origins of lacteal-associated axial SMC remain unexplored. We demonstrate that axial SMCs do not appear to be continuous with the submucosal lymphatic vasculature, which is devoid of muscle coverage (Miller et al., 2010). Instead, we suggest that axial SMCs arise from villous star-like progenitors associated with blood capillaries, regulated by *ASE*. In adult vessels, differentiated muscles are not proliferative and express unique contractile proteins (Gomez et al., 2015; Wang et al., 2015) reminiscent to axial SMCs. In contrast, the proliferative αSMA^{+} star cells show weak immunoreactivity for αSMA and Myh11, a progenitor-like phenotype. A few αSMA^{+} star cells remain in WT villi (Figure S4D). It is also conceivable that star-like progenitors remain in the villus but lose αSMA expression, akin to SMC phenotypic switching (Owens, 1995; Owens et al., 2004), and become undetectable by smooth muscle markers. We speculate that these cells may contribute to postnatal development or regeneration.

The transition from αSMA^{+} star to elongated spindle-like αSMA^{++} cells coincided with the appearance of lacteals (E18.5), implying lacteal-axial SMC crosstalk. Postnatal lacteals in WT and *Pitx2*$^{ASE/ASE}$ intestines always appeared with adjacent axial SMCs. Conversely, mispatterned axial SMCs with aberrant interconnecting branches were occasionally observed in *Pitx2*$^{ASE/ASE}$ villi without lacteals (Figure 3B). This suggests that axial SMCs are necessary for lacteal formation, whereas lacteals are required for SMC organization. Here we reveal the interplay between lacteal and axial SMC development during the pre- to postnatal transition that is *ASE* dependent.

Pitx2-mediated changes in ROS levels in the intestinal muscle

Oxidative stress is known to inhibit mesenteric lymphatic contractility and reduce lymph flow by affecting lymphatic smooth muscles (Thangaswamy et al., 2012; Zawieja et al., 1991). Our studies suggest that increased oxidative stress causes muscular-lacteal impairment in *Pitx2*$^{ASE/ASE}$ intestines, pointing to a crucial role of *Pitx2* in control of embryonic redox balance. During myogenesis, the post-mitotic transition of progenitors to mature contractile muscle involves a glycolytic-to-oxidative metabolic switch that increases ROS output (Blanchet et al., 2011; Remels et al., 2010). A network of antioxidant genes is critical to mitigate excessive ROS (Mittler, 2017; Schieber and Chandel, 2014). Recent work described an essential role of *Pitx2* and *Pitx3* in redox balance among differentiating myoblasts and satellite stem cells (L'honoré et al., 2014, 2018). Similarly, *Pitx2* maintains cardiac cellular composition during heart regeneration by preserving mitochondrial function (Li et al., 2018). In a neonatal cardiac injury model, *Pitx2c* has been shown to promote heart repair by activating the antioxidant response and ROS scavenger genes (Tao et al., 2016). We propose that *Pitx2* manages redox homeostasis in the developing gut.

Proteins are vulnerable to oxidation, depending on their structure and amino acid composition, affording specificity in post-translational ROS regulation. Although carbonylated proteins are cleared by the proteasome, oxidative stress can impede this process and prolong the half-life of carbonylated proteins (Grune et al., 2004; Stadtman and Levine, 2000), causing sublethal functional impairment and lesions such as actin aggregation (Castro et al., 2012; Dalle-Donne et al., 2001). We observed fragmented αSMA patterns in *Pitx2*$^{ASE/ASE}$ axial SMCs at P21 (Figure S5C) and profound villus smooth muscle hypoplasia at P26 (Figure S3B). Our data suggest that Pitx2-mediated control of ROS is critical to maintain dynamic organization of the actin cytoskeleton during organogenesis and in differentiated muscles. These data implicate Pitx2 as a rheostat of redox status during muscle development, inviting future studies that should define the roles of *Pitx2c* in smooth muscle regeneration after intestinal damage.

Pitx2 regulates lacteal development and function in a non-cell autonomous manner

Lymphatic function depends on the microenvironment (Bernier-Latmani et al., 2015; Davis et al., 2017; Hong et al., 2020; Nurmi et al., 2015; Petrova and Koh, 2018). Although ROS can act on nearby cells with (Niethammer et al., 2009; Yoo et al., 2011) or without (Lim et al., 2014) diffusion, ROS-generating axial SMCs can influence adjacent lacteal filopodium behavior. Filopodia are formed by linear polymerization of G-actin-ATP at their barbed ends, whereas filopodia actin bundle dynamics are regulated by ROS (Mattila and Lappalainen, 2008; Munnamalai and Suter, 2009; Shneyer et al., 2017). Lacteal filopodia ensure lacteal function and are crucial for LEC sprouting, extension, and regeneration (Bernier-Latmani et al., 2015; Xu et al., 2010). During adult lacteal regeneration, filopodium-mediated lacteal migration is regulated by the Notch ligand delta-like 4 (DLL4), downstream of VEGF-C (Bernier-Latmani et al., 2015). Deletion of DLL4 in LECs (Bernier-Latmani et al., 2015) or postnatal deletion of VEGF-C (Nurmi et al., 2015) leads to lacteal regression and impaired fat uptake, where VEGFR-3 interaction with NRP2 mediates lacteal sprouting in response to VEGF-C (Xu et al., 2010). Interestingly, we identified three highly conserved *Pitx2* binding regions upstream of the *VegfC* transcriptional start site and found reduced *VegfC* expression in *Pitx2*$^{ASE/ASE}$ embryos by E10.75 (data not shown). Our data suggest that Pitx2 provides the context of how the lymphangiogenic VEGF-C/R3 signaling is integrated with the body and organ plan. Collectively, elevated levels of ROS and reduced VEGF-C/R3 signaling in the absence of *ASE* may compromise filopodium-mediated lacteal extension, causing shorter lacteals and impaired dietary fat uptake and/or trafficking (Figure S9).

Pitx2$^{ASE/ASE}$ mice develop diet-induced fatty liver disease

The portal lipid transport is insignificant compared with the lymphatic pathway but increases during disease where lymphatic clearance is impaired (Cabré et al., 2005; Courtney and Warner, 2017; Fujimoto et al., 1991; Kurtel et al., 1991; Onufer et al., 2019). Lymphatic transport distributes dietary lipids to peripheral tissues for direct energy consumption, whereas the lymphatic system-independent portal route delivers lipids to the liver and reduces accessibility to peripheral tissues.

In our model, lymphatic lipid transport dominates in WT neonates, whereas muscular-lacteal defects in the absence of *ASE* cause lymphatic insufficiency. Compensatory activation of lymphatic system-independent (portal) lipid trafficking overwhelms hepatocytes and causes fatty liver in neonatal $Pitx2^{ASE/ASE}$ mice. Interestingly, these lesions resolved when $Pitx2^{ASE/ASE}$ weanlings transitioned to a low-fat diet. This suggests that non-alcoholic fatty liver disease (NAFLD) may be reversible with early diet adjustments, whereas a prolonged high-fat diet may lead to non-alcoholic steatohepatitis (NASH). These questions require further study using targeted mouse models.

The mechanism of portal lipid circulation in $Pitx2^{ASE/ASE}$ intestine is a key outstanding question. The liver is primarily perfused via the portal vein, and portal venous cargo strongly affects hepatic function (as in first-pass drug metabolism). Fatty acids and other nutrients, including carbohydrates and amino acids, are absorbed by enterocytes, a function that is broadly zonated along the villus axis, where genes associated with chylomicron packaging and lipid transport are most highly expressed in the tip-most enterocytes (Moor et al., 2018). This produces a chylomicron concentration gradient along the villus, affording chylomicrons priority access to taller lacteals (Takahara et al., 2013). Although chylomicrons are assumed to be too large to enter blood capillaries, smaller chylomicrons have been detected in hepatic portal blood (Takahara et al., 2013), perhaps via the fenestrated venous vasculature of the villi that may admit smaller lipoprotein particles (Furuya and Furuya, 2007). It is also well established that smaller lipoprotein particles (very-low-density lipoproteins [VLDLs], low-density lipoproteins [LDLs], and high-density lipoproteins [HDLs]) that routinely transit the lymphatic system-independent portal route (Hussain, 2014; Kindel et al., 2010) also participate in dietary lipid uptake. This becomes more evident in disease conditions of mice, rats, and humans (Anwar et al., 2007; Cabré et al., 2005; Courtney and Warner, 2017; Ee et al., 2000; Fujimoto et al., 1991; Hussain, 2014; Kurtel et al., 1991; McDonald et al., 1980; Onufer et al., 2019; Young et al., 1995) and may similarly contribute to lipid transport in *ASE* mice. Finally, fenestration pore sizes of blood capillaries may be altered in *ASE* mice, favoring chylomicron uptake, but that possibility has not been addressed in this work.

Fatty liver disease remains the single most common chronic liver disease worldwide (Tesfay et al., 2018). Our study provides one possible etiology–defective gut lymphatic development and intestinal fat transport–pointing to a role of *Pitx2*-driven organ laterality in regulating the gut-liver axis. This understanding may drive future discoveries of clinical targets involving alternative fat absorption pathways. Our findings unravel a role of the LR gene *Pitx2* during muscular-lacteal morphogenesis and reinforce the importance of the reciprocal interplay between intestinal muscle development and lacteal function in dietary lipid transport.

Limitations of the study

Loss of *Pitx2* results in early embryonic lethality and hampers postnatal studies. To circumvent this, we have leveraged the hypomorphic *ASE* allele and uncovered that *Pitx2* protects against fatty liver disease. The low postnatal survival rate and global loss of *ASE* have limited our interpretation of detailed molecular pathogenesis. In this regard, an inducible lineage-specific *Pitx2* knockout model is needed to precisely parse out the

mechanisms downstream of *Pitx2*. The major challenge in building this model is the lack of appropriate genetic tools that can dissect the roles of lymphatic and gut biology and the remaining questions about the cell of origin and developmental program of lacteal-associated SMCs. Our future work centers on generating gene expression maps of all intestinal cell types at single-cell resolution and across key stages to develop tools that will delete *Pitx2* with spatiotemporal precision.

Although the role of *Pitx2* in muscular redox homeostasis is well documented (L'honoré et al., 2014, 2018; Tao et al., 2016), the precise source of ROS causing oxidative damage in our model remains unclear. Moreover, the unstable nature of ROS escalates the challenge to capture real-time ROS production as well as the source of origin *in vivo*. We measured protein carbonylation instead as a functional readout of irreversible oxidative damage. However, protein carbonyl is a non-specific marker for protein oxidative damage, which provides limited information regarding the origin of ROS and the nature of oxidized protein. Biochemical analyses of sorted cell populations are needed to identify ROS origins and specific targets to better scrutinize the link between *Pitx2* and intestinal lymphatic function.

STAR★METHODS

RESOURCE AVAILABILITY

Lead contact—Further information and requests for resources and reagents should be directed to and will be fulfilled by the Lead Contact, Natasza A. Kurpios (natasza.kurpios@cornell.edu).

Materials availability—This study did not generate new unique reagents.

Data and code availability—The RNaseq database generated during this study is available at GEO: GSE160677

This paper does not report original code

Any additional information required to reanalyze the data reported in this paper is available from the lead contact upon request

EXPERIMENTAL MODEL AND SUBJECT DETAILS

All experiments adhered to guidelines of the Institutional Animal Care and Use Committee of Cornell University, under the Animal Welfare Assurance on file with the Office of Laboratory Animal Welfare. $Pitx2^{ASE/ASE}$, $Pitx2^{\Delta C}$, $Pitx2^{cre}$, ASE^{cre}, $ROSA26^{CAG\text{-}tdTomato}$, and ROSA26-EYFP mice were previously described (Liu et al., 2001,2002; Madisen et al., 2010; Shiratori et al., 2006; Srinivas et al., 2001). All strains of mice in these studies were maintained in a specified pathogen-free barrier facility under a 12-hour light cycle with free access to standard chow pellets and water unless specified. All mice used for mating were between 2-6 months old. For timed pregnancies, dams and studs were housed separately until the scheduled mating. Time mated breeding pairs were separated upon the morning when vaginal plugs were found and staged as E0.5. Postnatal stages are defined upon birth as postnatal day 0 (P0). Each mouse used was numbered by toe clip and genotyped by PCR

amplification at the age between 7-10 days. Embryos and pups under 9 days were genotyped after isolation. For full list of genotyping primers, see Supplemental Table. Each group of comparison contained at least three mice from representative genotypes at the specified developmental stages. Mice of different genotypes and gender were randomly chosen and sorted into different procedures and measurements. When possible, littermates of different genotypes were sorted into the same procedure and measurements as pairs.

METHOD DETAILS

Mouse tissue collection, fixation, processing—For sectioning, tissues were dissected in ice-cold 1X PBS, immediately followed by PBS washes and fixed overnight at 4°C in 4% paraformaldehyde (PFA)/PBS, ice-cold 100% MeOH, or PAXgene® fixative. For tissues fixed in PFA, tissues were thoroughly washed with PBS, then preserved in 4°C until use. Tissues fixed in MeOH were stored in −20°C until further use. Tissues fixed with PAXgene® fixative were processed following manufacturer's instructions. For intestinal tissue that proceeded to frozen sections, tissues were dehydrated in gradient sucrose/PBS solution, then embedded in Tissue-Tek* OCT. Compound and stored in −80°C until sectioning. Hepatic tissue for frozen sections following oil red O stain was embedded in 100% OCT immediately after dissection. Tissues intended for histology analyses were processed with standard paraffin embedding protocol in the Animal Health Diagnosis Center, Cornell University College of Veterinary Medicine. All frozen sections were 15 μm thick; paraffin sections were 5 μm thick.

Section and whole mount immunofluorescence—Embryos were processed for immunofluorescence (IF) on sections or whole mount (tissue slice). For section IF, frozen sections were permeabilized with 0.1% Triton X-100/PBS for 45 min, blocked in 3% BSA in PBS for 3 hours at room temperature, and incubated with 100X diluted primary antibodies/blocking overnight at room temperature. 500X diluted secondary antibodies were co-incubated with 1000x diluted DAPI for nuclear labeling at room temperature for 1 hour. Samples were mounted in ProLong™ Gold Antifade Mountant (P36930, Thermo Fisher) and preserved in room temperature until imaging. For whole mount IF staining, the protocol was adapted from (Bernier-Latmani and Petrova, 2016). In brief, tissue was blocked in BSA, serum, and 0.3% Triton X-100 in PBS in 4°C for 3 hours, then incubated with primary antibodies overnight at 4°C. Tissues were thoroughly washed in 0.3% Triton X-100/PBS for 5 hours with hourly buffer changes, then incubated with secondary antibody overnight at 4°C. Tissue was thoroughly washed in 0.3% Triton X-100/PBS for 5 hours with buffer changes every half hour, then fixed in 4% PFA/PBS for two overnights at 4°C. For confocal imaging, tissue was washed with PBS and properly sliced to 100-200 μm with spring scissors before mounted in ProLong™ Gold Antifade Mountant. Primary antibodies are listed below: GFP (ab290, Abcam), CD31 (PECAM-1, 553371, BD Bioscience), Lyve-1 (Ab14917, Abcam), αSMA (F3777, C6198, A2547, Sigma-Aldrich), and Myh11 (BT-563, Alfa Aesar). Secondary antibodies used are listed below: AlexaFluor anti-goat, anti-mouse or anti-rabbit 568, and anti-rabbit 488 (source).

Liver oil red O stain—Oil red O stain was performed to detect liver neutral lipids as previously described (Mehlem et al., 2013). In brief, tissue sections were processed as

described in the previous section. Slides with paired tissues from WT and *Pitx2*$^{ASE/ASE}$ littermates collected on the same slide were equivalate to room temperature from −80°C when stored, following oil red O and hematoxylin incubation. Slides were rinsed in water before mounted in MOWIOL® 4-88 Reagent (EM475904, EMD Millipore).

***In vivo* lipid tracer feeding assay—**BODIPY™FL C16 (Thermo Fisher D3821) was added to a warmed Intralipid (20% emulsion, Sigma I141) solubilizing agent to make final concentration at 0.4 μg/μl. 50 μL of 37°C reconstituted Bodipy™/Intralipid solution was fed to each pup through 24-gauge reusable feeding needles (Fine Science Tools 18061-24). To maintain proper body temperature and hydration, the pups were left with the dam for 5 hours (milk *ad lib*) before imaging and tissue collection. Of note, 2 hours was not sufficient for the *ASE* mixed strain background (C57BL/6 x C3H, mutant or WT) to see BODIPY. For both WT and ASE mice, 4-5 hours was the shortest time needed to detect BODIPY signal reaching ileum and the ileal mesenteric lymphatics. Images were taken under a Zeiss dissection microscope immediately after sacrifice by decapitation. Images were taken from liver tissue flash frozen in liquid nitrogen, then cryo-sectioned at 20 μm and mounted in ProLong™ Gold Antifade Mountant.

Tissue carbonyl assay detection—Protein Carbonyl Colorimetric Assay Kit (Cayman 10005020) was adapted for intestinal protein carbonyl measurement. In brief, small intestines were collected from animals euthanized by hypothermia followed by PBS perfusion. Intestine contents were removed by gentle swirling in ice-cold PBS after exposing the interior. Liquids were removed as much as possible before flash freezing the tissue in liquid nitrogen. 150 mg of tissue was homogenized in 50 mM phosphate buffer pH 6.7 then centrifuged at 10,000 x g for 15 min at 4°C. Supernatants were collected and incubated with 1% streptomycin sfate in 50mM potassium phosphate pH 7.2 at room temperature following centrifugation at 6,000 x g for 10 min at 4°C to remove excessive nucleic acids. Supernatants were collected and stored in −80°C until further use. The tissue carbonyl assay was then performed and analyzed following manual instruction.

Carbonylated total protein and smooth muscle actin-alpha measurement—EZ-link hydrazine-biotin was used to label protein carbonyl as previously described (Grimsrud et al., 2007; Xu et al., 2014b). Small intestines were collected in ice-cold PBS following removal of intestinal contents. Tissues were stored in −80°C until further processed. In brief, tissues were homogenized in ice-cold homogeneous buffer (pH5.5-100mM sodium acetate, 20mM NaCl, 0.1mM EDTA with protease and phosphatase inhibitor cocktail). Supernatant was incubated with 2% SDS in homogeneous buffer in 65°C for 5 min after centrifugation at 1200 rpm for 10 min in 4°C. Samples were further centrifuged at 13,000 g for 1 hour in 4°C. Supernatant was collected for protein concentration measurement and 100-150 μg of protein samples were then incubated with EZ-link hydrazine-biotin at 125uM for 2 hours at room temperature with constant mixing. Hydrazine-labeled samples were then dialyzed into PBS for streptavidin pulldown or αSMA IP. Specific bands of hydrazine-labeled proteins and αSMA were detected by western blot: samples were separated on SDS-PAGE then transferred to nitrocellulose membrane following 5% BSA blocking at room temperature for 1 hour before primary antibody or HRP-streptavidin incubation at 4°C overnight. For

αSMA detection, HRP-conjugated secondary antibody was incubated at room temperature for 1 hour before signal detection.

Liver Lipid Analysis—20 mg of fresh liver samples were flash frozen and homogenized in 1.8 mL of Chloroform: Methanol (2:1 v/v). The homogenates were centrifuged at 4000 rpm for 10 min. the Supernatants were collected into a clean tube and vortexed with 250 μl of 50mM NaCl. After 30 min of phases separation, 100 μL of lower phase extract was collected and mixed with 20 μL of Triton X-100/Chloroform mixture. The samples were then air-dried on 37°C heat block for 1 hour before resuspension in 80 μL of ddH_2O. 10 μl extract were used in the Serum Triglyceride Determination Kit from Sigma-Aldrich (TR0100) to determine hepatic triglyceride level. Hepatic neutral lipid accumulation was evaluated by Oil Red O stain as previously described (Mehlem et al., 2013). 10 μm frozen section tissues were stained with Oil Red O working solution prepared as described for 5 min, following Hematoxylin Solution, Mayer's (MHS1, Sigma-Aldrich) stain for 15 s. Tissue slides were rinsed in running tap water for 15-30 min until they were ready to mount in Gelvatol mounting medium. The Oil Red O stained slides were then imaged the following day.

Transmission electron microscopy—Tissues were isolated in ice-cold PBS and gently agitated to remove blood. Liver tissues were cut into approximately 1mm size cubes and fixed in 2% Glutaraldehyde, 2% Paraformaldehyde in 0.1M Sorensen's Phosphate Buffer overnight in 4°C then washed in ice-cold PBS 3 times. Tissues were then post fixed in 1% Osmium Tetroxide aqueous for 1 hour before they were dehydrated in graded ethanol series following Propylene Oxide washes and immersed in Araldite/Propylene Oxide 1:1 solution overnight. The samples were then soaked in fresh Araldite for 4 hours before final embedding and heated to polymerize *in silicon* rubber molds. Thin sections (60-90nm) were cut on a Leica EM UC6 Ultramicrotome. Sections were collected onto 200 mesh copper grids and stained with 2% Uranyl Acetate and Reynold's Lead Citrate before examined on the FEI Tecnai G2 Spirit Transmission Electron Microscope operated at 80 Kv.

RNA-sequencing—4 WT and 3 $Pitx2^{ASE/ASE}$ P1.5 small intestines were included in the analysis. Total RNA was isolated with Trizol, with an extra chloroform extraction to remove residual phenol and addition of glyco-blue as a carrier to promote RNA precipitation. RNA concentration was determined on a Nanodrop. TruSeq-barcoded RNA libraries were generated with the NEBNext Ultra II Directional RNA Library Prep Kit (New England Biolabs) with polyA+ enrichment using 1 μg total RNA as input. The libraries were sequenced on a NextSeq500 with single-end 85nt reads. Illumina pipeline software v1.8 was used for base calling. Trim_galore was used to trim and filter reads (–nextseq 20–length 50). STAR was used to map reads to the *Mus musculus* mm10 reference using Ensembl gene annotations and output raw counts (–quantMode GeneCounts). Differential gene expression was defined by false discovery rate (FDR, adjusted p value for multiple tests) ≤ 0.05 from raw counts between WT and $Pitx2^{ASE/ASE}$.

Gene Set Enrichment Analysis—All RNA-seq data from 4 WT and 3 $Pitx2^{ASE/ASE}$ P1.5 small intestines were included in the Hallmark gene sets v7.4 analysis from Molecular

Signatures Database (MSigDB). The following parameters were used to generate Figure S5A: Number of permutations = 1000, Permutation type = phenotype, Enrichment statistic = weighted, Metric for ranking genes = Signal2Noise.

QUANTIFICATION AND STATISTICAL ANALYSIS

Imaging and quantifications—Microscopic images were acquired using a Zeiss Observer.Z1/Apotome. Confocal images were taken on Zeiss LSM880 confocal microscopes. To capture the entire lacteal and villus in whole mount immunofluorescent stain, multiple adjacent fields of images were taken under a 40X lens then stitched on Zen before exporting for further analyses. Imaris 9.5 was used for image processing, filtering, background subtraction, confocal image stacking, and quantifications. Measurements (lacteal length, filopodia counts etc.) were done on Imaris 9.5 or Fiji. Z stack images were all analyzed on Imaris 9.5.

Statistics—Statistical analyses were performed in GraphPad Prism 8 (La Jolla, CA). Comparison between different genotypes were tested by unpaired, two tailed Student's t test. All data were first analyzed as mean values of measurements (lacteal length, filopodia number, etc.) from multiple villi in multiple fields across the proximal small intestine for each animal. Lacteal filopodium was defined as cell protrusion longer than or equal to 6 μm. The mean values from all animals were then plotted in groups based on genotype and developmental stages. Almost all data were expressed as mean of the means from each mouse ± standard error of mean (SEM).

Supplementary Material

Refer to Web version on PubMed Central for supplementary material.

ACKNOWLEDGMENTS

We thank Kurpios lab members and Dr. D. Gludish for reading the manuscript. We thank Drs. H. Hamada, J. Martin, and T. Tumbar for reagents. We thank T. Bargar and N. Conoan for EM technical assistance, supported by the Nebraska Research Initiative, University of Nebraska Foundation, and the Office of the Vice Chancellor for Research. We are grateful to A. VanDeMark for help with mouse feeding, Drs. J. Dela Cruz and R. Williams for imaging expertise, A. Sulpizio for lipid quantification, and Drs. T. Stokol, E. Behling-Kelly, T. Southard, and S. Center for clinical discussions. We thank Dr. J. Grenier of the Cornell Institute of Biotechnology for RNA-seq analysis and R. Munroe and C. Abratte of the Cornell Stem Cell and Transgenic Core Facility. We are grateful to B. Laslow, R. Slater, and C. Westmiller for technical assistance. Imaging data were acquired through the Cornell BRC Imaging Facility, with NYSTEM (C029155) and NIH (S10OD018516) funding for the shared Zeiss LSM880 confocal/multiphoton microscope. The NIH-funded Comparative Medicine Training Program T32OD011000 (to S.H.), AHA 17SDG33400141 (to G.T.), and NIDDK R01 DK107634 and DK092776 (to N.A.K.) supported this work.

REFERENCES

Adams RH, and Alitalo K (2007). Molecular regulation of angiogenesis and lymphangiogenesis. Nat. Rev. Mol. Cell Biol 8, 464–478. [PubMed: 17522591]

Airik R, Bussen M, Singh MK, Petry M, and Kispert A (2006). Tbx18 regulates the development of the ureteral mesenchyme. J. Clin. Invest 116, 663–674. [PubMed: 16511601]

Alexander JS, Chaitanya GV, Grisham MB, and Boktor M (2010a). Emerging roles of lymphatics in inflammatory bowel disease. Ann. N Y Acad. Sci 1207 (Suppl 1), E75–E85. [PubMed: 20961310]

Alexander JS, Ganta VC, Jordan PA, and Witte MH (2010b). Gastrointestinal lymphatics in health and disease. Pathophysiology 17, 315–335. [PubMed: 20022228]

Alitalo K (2011). The lymphatic vasculature in disease. Nat. Med 17, 1371–1380. [PubMed: 22064427]

Alitalo K, Tammela T, and Petrova TV (2005). Lymphangiogenesis in development and human disease. Nature 438, 946–953. [PubMed: 16355212]

Anwar K, Iqbal J, and Hussain MM (2007). Mechanisms involved in vitamin E transport by primary enterocytes and in vivo absorption. J. Lipid Res 48, 2028–2038. [PubMed: 17582142]

Bernier-Latmani J, and Petrova TV (2016). High-resolution 3D analysis of mouse small-intestinal stroma. Nat. Protoc 11, 1617–1629. [PubMed: 27560169]

Bernier-Latmani J, and Petrova TV (2017). Intestinal lymphatic vasculature: structure, mechanisms and functions. Nat. Rev. Gastroenterol. Hepatol 14, 510–526. [PubMed: 28655884]

Bernier-Latmani J, Cisarovsky C, Demir CS, Bruand M, Jaquet M, Davanture S, Ragusa S, Siegert S, Dormond O, Benedito R, et al. (2015). DLL4 promotes continuous adult intestinal lacteal regeneration and dietary fat transport. J. Clin. Invest 125, 4572–586. [PubMed: 26529256]

Betterman KL, and Harvey NL (2016). The lymphatic vasculature: development and role in shaping immunity. Immunol. Rev 271, 276–292. [PubMed: 27088921]

Blanchet E, Annicotte JS, Lagarrigue S, Aguilar V, Clapé C, Chavey C, Fritz V, Casas F, Apparailly F, Auwerx J, and Fajas L (2011). E2F transcription factor-1 regulates oxidative metabolism. Nat. Cell Biol 13, 1146–1152. [PubMed: 21841792]

Cabré E, Hernández-Pérez JM, Fluvià L, Pastor C, Corominas A, and Gassull MA (2005). Absorption and transport of dietary long-chain fatty acids in cirrhosis: a stable-isotope-tracing study. Am. J. Clin. Nutr 81, 692–701. [PubMed: 15755841]

Campione M, Steinbeisser H, Schweickert A, Deissler K, van Bebber F, Lowe LA, Nowotschin S, Viebahn C, Haffter P, Kuehn MR, and Blum M (1999). The homeobox gene Pitx2: mediator of asymmetric left-right signaling in vertebrate heart and gut looping. Development 126, 1225–1234. [PubMed: 10021341]

Castro JP, Ott C, Jung T, Grune T, and Almeida H (2012). Carbonylation of the cytoskeletal protein actin leads to aggregate formation. Free Radic. Biol. Med 53, 916–925. [PubMed: 22705366]

Chevion M, Berenshtein E, and Stadtman ER (2000). Human studies related to protein oxidation: protein carbonyl content as a marker of damage. Free Radic. Res 33 (Suppl), S99–S108. [PubMed: 11191280]

Choe K, Jang JY, Park I, Kim Y, Ahn S, Park DY, Hong YK, Alitalo K, Koh GY, and Kim P (2015). Intravital imaging of intestinal lacteals unveils lipid drainage through contractility. J. Clin. Invest 125, 4042–4052. [PubMed: 26436648]

Cifarelli V, and Eichmann A (2019). The Intestinal Lymphatic System: Functions and Metabolic Implications. Cell. Mol. Gastroenterol. Hepatol 7, 503–513. [PubMed: 30557701]

Courtney CM, and Warner BW (2017). Pediatric intestinal failure-associated liver disease. Curr. Opin. Pediatr 29, 363–370. [PubMed: 28333693]

Cueni LN, and Detmar M (2008). The lymphatic system in health and disease. Lymphat. Res. Biol 6, 109–122. [PubMed: 19093783]

Dalle-Donne I, Rossi R, Giustarini D, Gagliano N, Lusini L, Milzani A, Di Simplicio P, and Colombo R (2001). Actin carbonylation: from a simple marker of protein oxidation to relevant signs of severe functional impairment. Free Radic. Biol. Med 31, 1075–1083. [PubMed: 11677040]

Dalle-Donne I, Rossi R, Giustarini D, Gagliano N, Di Simplicio P, Colombo R, and Milzani A (2002). Methionine oxidation as a major cause of the functional impairment of oxidized actin. Free Radic. Biol. Med 32, 927–937. [PubMed: 11978495]

Dalle-Donne I, Giustarini D, Rossi R, Colombo R, and Milzani A (2003a). Reversible S-glutathionylation of Cys 374 regulates actin filament formation by inducing structural changes in the actin molecule. Free Radic. Biol. Med 34, 23–32. [PubMed: 12498976]

Dalle-Donne I, Rossi R, Giustarini D, Milzani A, and Colombo R (2003b). Protein carbonyl groups as biomarkers of oxidative stress. Clin. Chim. Acta 329, 23–38. [PubMed: 12589963]

Davis NM, Kurpios NA, Sun X, Gros J, Martin JF, and Tabin CJ (2008). The chirality of gut rotation derives from left-right asymmetric changes in the architecture ofthe dorsal mesentery. Dev. Cell 15, 134–145. [PubMed: 18606147]

Davis RB, Kechele DO, Blakeney ES, Pawlak JB, and Caron KM (2017). Lymphatic deletion of calcitonin receptor-like receptor exacerbates intestinal inflammation. JCI Insight 2, e92465. [PubMed: 28352669]

Dixit M, Ansseau E, Tassin A, Winokur S, Shi R, Qian H, Sauvage S, Mattéotti C, van Acker AM, Leo O, et al. (2007). DUX4, a candidate gene of facioscapulohumeral muscular dystrophy, encodes a transcriptional activator of PITX1. Proc. Natl. Acad. Sci. USA 104, 18157–18162. [PubMed: 17984056]

Dixon JB (2010). Mechanisms of chylomicron uptake into lacteals. Ann. N Y Acad. Sci 1207 (Suppl 1), E52–E57. [PubMed: 20961306]

Dixon JB, Raghunathan S, and Swartz MA (2009). A tissue-engineered model of the intestinal lacteal for evaluating lipid transport by lymphatics. Bio-technol. Bioeng 103, 1224–1235.

Ee LC, Zheng S, Yao L, and Tso P (2000). Lymphatic absorption of fatty acids and cholesterol in the neonatal rat. Am. J. Physiol. Gastrointest. Liver Physiol 279, G325–G331. [PubMed: 10915641]

Fedorova M, Bollineni RC, and Hoffmann R (2014). Protein carbonylation as a major hallmark of oxidative damage: update of analytical strategies. Mass Spectrom. Rev 33, 79–97. [PubMed: 23832618]

Fujimoto K, Price VH, Granger DN, Specian R, Bergstedt S, and Tso P (1991). Effect of ischemia-reperfusion on lipid digestion and absorption in rat intestine. Am. J. Physiol 260, G595–G602. [PubMed: 2018134]

Furuya S, and Furuya K (2007). Subepithelial fibroblasts in intestinal villi: roles in intercellular communication. Int. Rev. Cytol 264, 165–223. [PubMed: 17964923]

Gomez D, Swiatlowska P, and Owens GK (2015). Epigenetic Control of Smooth Muscle Cell Identity and Lineage Memory. Arterioscler. Thromb. Vasc. Biol 35, 2508–2516. [PubMed: 26449751]

Görs S, Kucia M, Langhammer M, Junghans P, and Metges CC (2009). Technical note: Milk composition in mice–methodological aspects and effects of mouse strain and lactation day. J. Dairy Sci 92, 632–637. [PubMed: 19164675]

Grimsrud PA, Picklo MJ Sr., Griffin TJ, and Bernlohr DA (2007). Carbonylation of adipose proteins in obesity and insulin resistance: identification of adipocyte fatty acid-binding protein as a cellular target of 4-hydroxynonenal. Mol. Cell. Proteomics 6, 624–637. [PubMed: 17205980]

Grune T, Jung T, Merker K, and Davies KJ (2004). Decreased proteolysis caused by protein aggregates, inclusion bodies, plaques, lipofuscin, ceroid, and 'aggresomes' during oxidative stress, aging, and disease. Int. J. Biochem. Cell Biol 36, 2519–2530. [PubMed: 15325589]

Güldner FH, Wolff JR, and Keyserlingk DG (1972). Fibroblasts as a part of the contractile system in duodenal villi of rat. Z. Zellforsch. Mikrosk. Anat 135, 349–360. [PubMed: 4345454]

Hong SP, Yang MJ, Cho H, Park I, Bae H, Choe K, Suh SH, Adams RH, Alitalo K, Lim D, and Koh GY (2020). Distinct fibroblast subsets regulate lacteal integrity through YAP/TAZ-induced VEGF-C in intestinal villi. Nat. Commun 11, 4102. [PubMed: 32796823]

Hosoyamada Y, and Sakai T (2007). Mechanical components of rat intestinal villi as revealed by ultrastructural analysis with special reference to the axial smooth muscle cells in the villi. Arch. Histol. Cytol 70, 107–116. [PubMed: 17827668]

Hung RJ, Pak CW, and Terman JR (2011). Direct redox regulation of F-actin assembly and disassembly by Mical. Science 334, 1710–1713. [PubMed: 22116028]

Hung RJ, Spaeth CS, Yesilyurt HG, and Terman JR (2013). SelR reverses Mical-mediated oxidation of actin to regulate F-actin dynamics. Nat. Cell Biol 15, 1445–1454. [PubMed: 24212093]

Hussain MM (2014). Intestinal lipid absorption and lipoprotein formation. Curr. Opin. Lipidol 25, 200–206. [PubMed: 24751933]

Huycke TR, Miller BM, Gill HK, Nerurkar NL, Sprinzak D, Mahadevan L, and Tabin CJ (2019). Genetic and Mechanical Regulation of Intestinal Smooth Muscle Development. Cell 179, 90–105.e21. [PubMed: 31539501]

Kim KE, Sung HK, and Koh GY (2007). Lymphatic development in mouse small intestine. Dev. Dyn 236, 2020–2025. [PubMed: 17576138]

Kindel T, Lee DM, and Tso P (2010). The mechanism of the formation and secretion of chylomicrons. Atheroscler. Suppl 11, 11–16. [PubMed: 20493784]

Ko CW, Qu J, Black DD, and Tso P (2020). Regulation of intestinal lipid metabolism: current concepts and relevance to disease. Nat. Rev. Gastroenterol. Hepatol 17, 169–183. [PubMed: 32015520]

Kurtel H, Fujimoto K, Zimmerman BJ, Granger DN, and Tso P (1991). Ischemia-reperfusion-induced mucosal dysfunction: role of neutrophils. Am. J. Physiol 261, G490–G496. [PubMed: 1887895]

L'honoré A, Ouimette JF, Lavertu-Jolin M, and Drouin J (2010). Pitx2 defines alternate pathways acting through MyoD during limb and somitic myogenesis. Development 137, 3847–3856. [PubMed: 20978076]

L'honoré A, Commère PH, Ouimette JF, Montarras D, Drouin J, and Buckingham M (2014). Redox regulation by Pitx2 and Pitx3 is critical for fetal myogenesis. Dev. Cell 29, 392–405. [PubMed: 24871946]

L'honoré A, Commère PH, Negroni E, Pallafacchina G, Friguet B, Drouin J, Buckingham M, and Montarras D (2018). The role of Pitx2 and Pitx3 in muscle stem cells gives new insights into P38α MAP kinase and redox regulation of muscle regeneration. eLife 7, e32991. [PubMed: 30106373]

Lagha M, Sato T, Regnault B, Cumano A, Zuniga A, Licht J, Relaix F, and Buckingham M (2010). Transcriptome analyses based on genetic screens for Pax3 myogenic targets in the mouse embryo. BMC Genomics 11, 696. [PubMed: 21143873]

Li L,Tao G, Hill MC, Zhang M, Morikawa Y, and Martin JF (2018). *Pitx2* maintains mitochondrial function during regeneration to prevent myocardial fat deposition. Development 145, dev168609. [PubMed: 30143541]

Lim HY, Wang W, Chen J, Ocorr K, and Bodmer R (2014). ROS regulate cardiac function via a distinct paracrine mechanism. Cell Rep 7, 35–44. [PubMed: 24656823]

Liu C, Liu W, Lu MF, Brown NA, and Martin JF (2001). Regulation of left-right asymmetry by thresholds of Pitx2c activity. Development 128, 2039–2048. [PubMed: 11493526]

Liu C, Liu W, Palie J, Lu MF, Brown NA, and Martin JF (2002). Pitx2c patterns anterior myocardium and aortic arch vessels and is required for local cell movement into atrioventricular cushions. Development 129, 5081–5091. [PubMed: 12397115]

Logan M, Pagán-Westphal SM, Smith DM, Paganessi L, and Tabin CJ (1998). The transcription factor Pitx2 mediates situs-specific morphogenesis in response to left-right asymmetric signals. Cell 94, 307–317. [PubMed: 9708733]

Lu SC (2013). Glutathione synthesis. Biochim. Biophys. Acta 1830, 3143–3153. [PubMed: 22995213]

Lu MF, Pressman C, Dyer R, Johnson RL, and Martin JF (1999). Function of Rieger syndrome gene in left-right asymmetry and craniofacial development. Nature 401, 276–278. [PubMed: 10499585]

Madisen L, Zwingman TA, Sunkin SM, Oh SW, Zariwala HA, Gu H, Ng LL, Palmiter RD, Hawrylycz MJ, Jones AR, et al. (2010). A robust and high-throughput Cre reporting and characterization system for the whole mouse brain. Nat. Neurosci 13, 133–140. [PubMed: 20023653]

Mahadevan A, Welsh IC, Sivakumar A, Gludish DW, Shilvock AR, Noden DM, Huss D, Lansford R, and Kurpios NA (2014). The left-right Pitx2 pathway drives organ-specific arterial and lymphatic development in the intestine. Dev. Cell 31, 690–706. [PubMed: 25482882]

Mattila PK, and Lappalainen P (2008). Filopodia: molecular architecture and cellular functions. Nat. Rev. Mol. Cell Biol 9, 446–454. [PubMed: 18464790]

McDonald GB, Saunders DR, Weidman M, and Fisher L (1980). Portal venous transport of long-chain fatty acids absorbed from rat intestine. Am. J. Physiol 239, G141–G150. [PubMed: 7435568]

Mehlem A, Hagberg CE, Muhl L, Eriksson U, and Falkevall A (2013). Imaging of neutral lipids by oil red O for analyzing the metabolic status in health and disease. Nat. Protoc 8, 1149–1154. [PubMed: 23702831]

Miller MJ, McDole JR, and Newberry RD (2010). Microanatomy of the intestinal lymphatic system. Ann. N Y Acad. Sci 1207 (Suppl 1), E21–E28. [PubMed: 20961303]

Mittler R (2017). ROS Are Good. Trends Plant Sci 22, 11–19. [PubMed: 27666517]

Moor AE, Harnik Y, Ben-Moshe S, Massasa EE, Rozenberg M, Eilam R, Bahar Halpern K, and Itzkovitz S (2018). Spatial Reconstruction of Single Enterocytes Uncovers Broad Zonation along the Intestinal Villus Axis. Cell 175, 1156–1167.e15. [PubMed: 30270040]

Munnamalai V, and Suter DM (2009). Reactive oxygen species regulate F-actin dynamics in neuronal growth cones and neurite outgrowth. J. Neurochem 108, 644–661. [PubMed: 19054285]

Niethammer P, Grabher C, Look AT, and Mitchison TJ (2009). A tissue-scale gradient of hydrogen peroxide mediates rapid wound detection in zebra-fish. Nature 459, 996–999. [PubMed: 19494811]

Nurmi H, Saharinen P, Zarkada G, Zheng W, Robciuc MR, and Alitalo K (2015). VEGF-C is required for intestinal lymphatic vessel maintenance and lipid absorption. EMBO Mol. Med 7, 1418–1425. [PubMed: 26459520]

Onufer EJ, Czepielewski R, Seiler KM, Erlich E, Courtney CM, Bustos A, Randolph GJ, and Warner BW (2019). Lymphatic network remodeling after small bowel resection. J. Pediatr. Surg 54, 1239–1244. [PubMed: 30879758]

Owens GK (1995). Regulation of differentiation of vascular smooth muscle cells. Physiol. Rev 75, 487–517. [PubMed: 7624392]

Owens GK, Kumar MS, and Wamhoff BR (2004). Molecular regulation of vascularsmooth muscle cell differentiation in development and disease. Physiol. Rev 84, 767–801. [PubMed: 15269336]

Petrova TV, and Koh GY (2018). Organ-specific lymphatic vasculature: From development to pathophysiology. J. Exp. Med 215, 35–49. [PubMed: 29242199]

Remels AH, Langen RC, Schrauwen P, Schaart G, Schols AM, and Gosker HR (2010). Regulation of mitochondrial biogenesis during myogenesis. Mol. Cell. Endocrinol 315, 113–120. [PubMed: 19804813]

Ryan AK, Blumberg B, Rodriguez-Esteban C, Yonei-Tamura S, Tamura K, Tsukui T, de la Peña J, Sabbagh W, Greenwald J, Choe S, et al. (1998). Pitx2 determines left-right asymmetry of internal organs in vertebrates. Nature 394, 545–551. [PubMed: 9707115]

Schieber M, and Chandel NS (2014). ROS function in redox signaling and oxidative stress. Curr. Biol 24, R453–R462. [PubMed: 24845678]

Schweickert A, Campione M 1, Steinbeisser H, and Blum M (2000). Pitx2 isoforms: involvement of Pitx2c but not Pitx2a or Pitx2b in vertebrate left-right asymmetry. Mech. Dev 90, 41–51. [PubMed: 10585561]

Semina EV, Reiter R, Leysens NJ, Alward WL, Small KW, Datson NA, Siegel-Bartelt J, Bierke-Nelson D, Bitoun P, Zabel BU, et al. (1996). Cloning and characterization of a novel bicoid-related homeobox transcription factor gene, RIEG, involved in Rieger syndrome. Nat. Genet 14, 392–399. [PubMed: 8944018]

Semina EV, Ferrell RE, Mintz-Hittner HA, Bitoun P, Alward WL, Reiter RS, Funkhauser C, Daack-Hirsch S, and Murray JC (1998). A novel homeobox gene PITX3 is mutated in families with autosomal-dominant cataracts and ASMD. Nat. Genet 19, 167–170. [PubMed: 9620774]

Shiratori H, Sakuma R, Watanabe M, Hashiguchi H, Mochida K, Sakai Y, Nishino J, Saijoh Y, Whitman M, and Hamada H (2001). Two-step regulation of left-right asymmetric expression of Pitx2: initiation by nodal signaling and maintenance by Nkx2. Mol. Cell 7, 137–149. [PubMed: 11172719]

Shiratori H, Yashiro K, Shen MM, and Hamada H (2006). Conserved regulation and role of Pitx2 in situs-specific morphogenesis of visceral organs. Development 133, 3015–3025. [PubMed: 16835440]

Shiratori H, Yashiro K, Iwai N, Oki S, Minegishi K, Ikawa Y, Kanata K, and Hamada H (2014). Self-regulated left-right asymmetric expression of Pitx2c in the developing mouse limb. Dev. Biol 395, 331–341. [PubMed: 25224222]

Shneyer BI, Ušaj M, Wiesel-Motiuk N, Regev R, and Henn A (2017). ROS induced distribution of mitochondria to filopodia by Myo19 depends on a class specific tryptophan in the motor domain. Sci. Rep 7, 11577. [PubMed: 28912530]

Srinivas S, Watanabe T, Lin CS, William CM, Tanabe Y, Jessell TM, and Costantini F (2001). Cre reporter strains produced by targeted insertion of EYFP and ECFP into the ROSA26 locus. BMC Dev. Biol 1, 4. [PubMed: 11299042]

Stadtman ER, and Levine RL (2000). Protein oxidation. Ann. N Y Acad. Sci 899, 191–208. [PubMed: 10863540]

Subramanian A, Tamayo P, Mootha VK, Mukherjee S, Ebert BL, Gillette MA, Paulovich A, Pomeroy SL, Golub TR, Lander ES, and Mesirov JP (2005). Gene set enrichment analysis: a knowledge-based approach for interpreting genome-wide expression profiles. Proc. Natl. Acad. Sci. USA 102, 15545–15550. [PubMed: 16199517]

Takahara E, Mantani Y, Udayanga KG, Qi WM, Tanida T, Takeuchi T, Yokoyama T, Hoshi N, and Kitagawa H (2013). Ultrastructural demonstration of the absorption and transportation of minute chylomicrons by subepithelial blood capillaries in rat jejunal villi. J. Vet. Med. Sci 75, 1563–1569. [PubMed: 23892460]

Tammela T, Zarkada G, Wallgard E, Murtomäki A, Suchting S, Wirzenius M, Waltari M, Hellström M, Schomber T, Peltonen R, et al. (2008). Blocking VEGFR-3 suppresses angiogenic sprouting and vascular network formation. Nature 454, 656–660. [PubMed: 18594512]

Tao G, Kahr PC, Morikawa Y, Zhang M, Rahmani M, Heallen TR, Li L, Sun Z, Olson EN, Amendt BA, and Martin JF (2016). Pitx2 promotes heart repair by activating the antioxidant response after cardiac injury. Nature 534, 119–123. [PubMed: 27251288]

Tesfay M, Goldkamp WJ, and Neuschwander-Tetri BA (2018). NASH: The Emerging Most Common Form of Chronic Liver Disease. Mo. Med 115, 225–229. [PubMed: 30228727]

Thangaswamy S, Bridenbaugh EA, and Gashev AA (2012). Evidence of increased oxidative stress in aged mesenteric lymphatic vessels. Lymphat. Res. Biol 10, 53–62. [PubMed: 22540739]

Trautman A (1909). Die Muskulatur in den Dünndarmzotten der Haustiere. Anat. Anz, 34.

Wang TY, Liu M, Portincasa P, and Wang DQ (2013). New insights into the molecular mechanism of intestinal fatty acid absorption. Eur. J. Clin. Invest 43, 1203–1223. [PubMed: 24102389]

Wang J, Bai Y, Li N, Ye W, Zhang M, Greene SB, Tao Y, Chen Y, Wehrens XH, and Martin JF (2014). Pitx2-microRNA pathway that delimits sinoatrial node development and inhibits predisposition to atrial fibrillation. Proc. Natl. Acad. Sci. USA 111, 9181–9186. [PubMed: 24927531]

Wang G, Jacquet L, Karamariti E, and Xu Q (2015). Origin and differentiation of vascular smooth muscle cells. J. Physiol 593, 3013–3030. [PubMed: 25952975]

Welsh IC, Thomsen M, Gludish DW, Alfonso-Parra C, Bai Y, Martin JF, and Kurpios NA (2013). Integration of left-right Pitx2 transcription and Wnt signaling drives asymmetric gut morphogenesis via Daam2. Dev. Cell 26, 629–644. [PubMed: 24091014]

Wilm B, Ipenberg A, Hastie ND, Burch JB, and Bader DM (2005). The serosal mesothelium is a major source of smooth muscle cells of the gut vasculature. Development 132, 5317–5328. [PubMed: 16284122]

Wilson C, and González-Billault C (2015). Regulation of cytoskeletal dynamics by redox signaling and oxidative stress: implications for neuronal development and trafficking. Front. Cell. Neurosci 9, 381. [PubMed: 26483635]

Winters NI,Williams AM, and Bader DM (2014). Resident progenitors, not exogenous migratory cells, generate the majority of visceral mesothelium in organogenesis. Dev. Biol 391, 125–132. [PubMed: 24746591]

Xu Y,Yuan L, Mak J, Pardanaud L, Caunt M, Kasman I, Larrivée B, Del Toro R, Suchting S, Medvinsky A, et al. (2010). Neuropilin-2 mediates VEGF-C-induced lymphatic sprouting together with VEGFR3. J. Cell Biol 188, 115–130. [PubMed: 20065093]

Xu J, Nie X, Cai X, Cai CL, and Xu PX (2014a). Tbx18 is essential for normal development of vasculature network and glomerular mesangium in the mammalian kidney. Dev. Biol 391, 17–31. [PubMed: 24727670]

Xu Q, Hahn WS, and Bernlohr DA (2014b). Detecting protein carbonylation in adipose tissue and in cultured adipocytes. Methods Enzymol 538, 249–261. [PubMed: 24529443]

Xu Q, Huff LP, Fujii M, and Griendling KK (2017). Redox regulation of the actin cytoskeleton and its role in the vascular system. Free Radic. Biol. Med 109, 84–107. [PubMed: 28285002]

Yoo SK, Starnes TW, Deng Q, and Huttenlocher A (2011). Lyn is a redox sensor that mediates leukocyte wound attraction in vivo. Nature 480, 109–112. [PubMed: 22101434]

Yoshioka H, Meno C, Koshiba K, Sugihara M, Itoh H, Ishimaru Y, Inoue T, Ohuchi H, Semina EV, Murray JC, et al. (1998). Pitx2, a bicoid-type homeobox gene, is involved in a lefty-signaling pathway in determination of left-right asymmetry. Cell 94, 299–305. [PubMed: 9708732]

Young SG, Cham CM, Pitas RE, Burri BJ, Connolly A, Flynn L, Pappu AS, Wong JS, Hamilton RL, and Farese RV Jr. (1995). A genetic model for absent chylomicron formation: mice producing apolipoprotein B in the liver, but not in the intestine. J. Clin. Invest 96, 2932–2946. [PubMed: 8675665]

Zawieja DC, Greiner ST, Davis KL, Hinds WM, and Granger HJ (1991). Reactive oxygen metabolites inhibit spontaneous lymphatic contractions. Am. J. Physiol 260, H1935–H1943. [PubMed: 2058726]

Zhang F, Zarkada G, Han J, Li J, Dubrac A, Ola R, Genet G, Boyé K, Michon P, Künzel SE, et al. (2018). Lacteal junction zippering protects against diet-induced obesity. Science 361, 599–603. [PubMed: 30093598]

Zhou Y, Liu D, and Kaminski HJ (2011). Pitx2 regulates myosin heavy chain isoform expression and multi-innervation in extraocular muscle. J. Physiol 589, 4601–4614. [PubMed: 21727215]

Zhou A, Qu J, Liu M, and Tso P (2020). The Role of Interstitial Matrix and the Lymphatic System in Gastrointestinal Lipid and Lipoprotein Metabolism. Front. Physiol 11, 4. [PubMed: 32038309]

Highlights

- Lacteal-associated smooth muscle requires *Pitx2*-driven LR asymmetry
- *ASE* deletion leads to redox imbalance in intestinal smooth muscle lineage
- *ASE* is required for the normal route of dietary lipid transport
- $Pitx2^{ASE/ASE}$ neonates develop diet-induced fatty liver disease

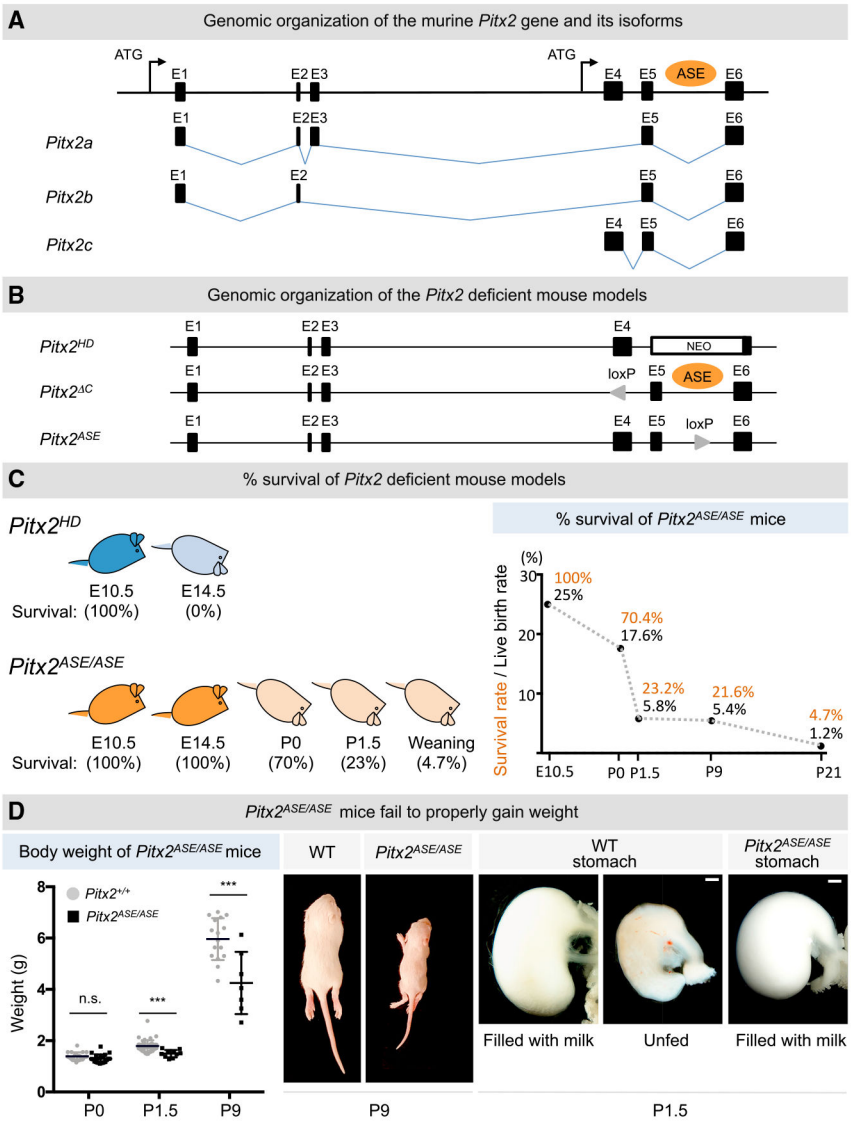

Figure 1. *Pitx2*$^{ASE/ASE}$ mice fail to properly gain weight

(A) *Pitx2* gene structure. E, exon; ATG, start codon; black arrow, transcriptional start site; ASE, asymmetric enhancer.

(B) Pitx2-deficient mouse models. *Pitx2*^{HD} has homeobox deletion from exon 5 to exon 6. *Pitx2*$^{\Delta C}$ has *Pitx2c*-specific exon 4 deletion. *Pitx2*^{ASE} contains *ASE* deletion in intron 5.

(C) Survival rates of *Pitx2*$^{ASE/ASE}$ mice. Data displayed on the y axis are represented as incidence of live *Pitx2*$^{ASE/ASE}$ mice on collection (n = 28 at E10.5, 125 at P0, 500 at P1.5, 533 at P9, and 169 at P21 [weaning age]). Orange marks, survival rate of *Pitx2*$^{ASE/ASE}$ mice based on the number of *Pitx2*$^{ASE/ASE}$ live mice/expected number of mice per Mendelian ratio (25%); black marks, live birth rate of *Pitx2*$^{ASE/ASE}$ mice based on the number of *Pitx2*$^{ASE/ASE}$ live mice/number of total live mice.

(D) *Pitx2*$^{ASE/ASE}$ mice show abnormal weight gain. Left: body weights measured at E18.5 and birth are counted as P0. Center: a pair of littermates showing significant growth retardation of *Pitx2*$^{ASE/ASE}$ versus the WT at P9. Right: stomach at collection of P1.5 WT

fed, WT unfed, and *Pitx2*$^{ASE/ASE}$ fed mates. Data displayed on the y axis in the left graph are represented as mean ± SEM. P0 WT = 1.388 ± 0.03382 g, n = 21; P0 *Pitx2*$^{ASE/ASE}$ = 1.295 ± 0.03531 g, n = 22. Difference between WT and *Pitx2*$^{ASE/ASE}$ = 0.09264 ± 0.04897 g, p = 0.0656. P1.5 WT = 1.791 ± 0.2251 g, n = 41; P1.5 *Pitx2*$^{ASE/ASE}$ = 1.495 ± 0.1435 g, n = 10. Difference between WT and *Pitx2*$^{ASE/ASE}$ = −0.2960 ± 0.07494 g, p = 0.0003***. P9WT = 5.963 ± 0.8161 g, n = 16; P9 *Pitx2*$^{ASE/ASE}$ = 4.25 ± 1.211 g, n = 7. Difference between WT and *Pitx2*$^{ASE/ASE}$ = −1.713 ± 0.4286 g, ***p = 0.0007. Scale bars, 500 μm. See also Figure S1.

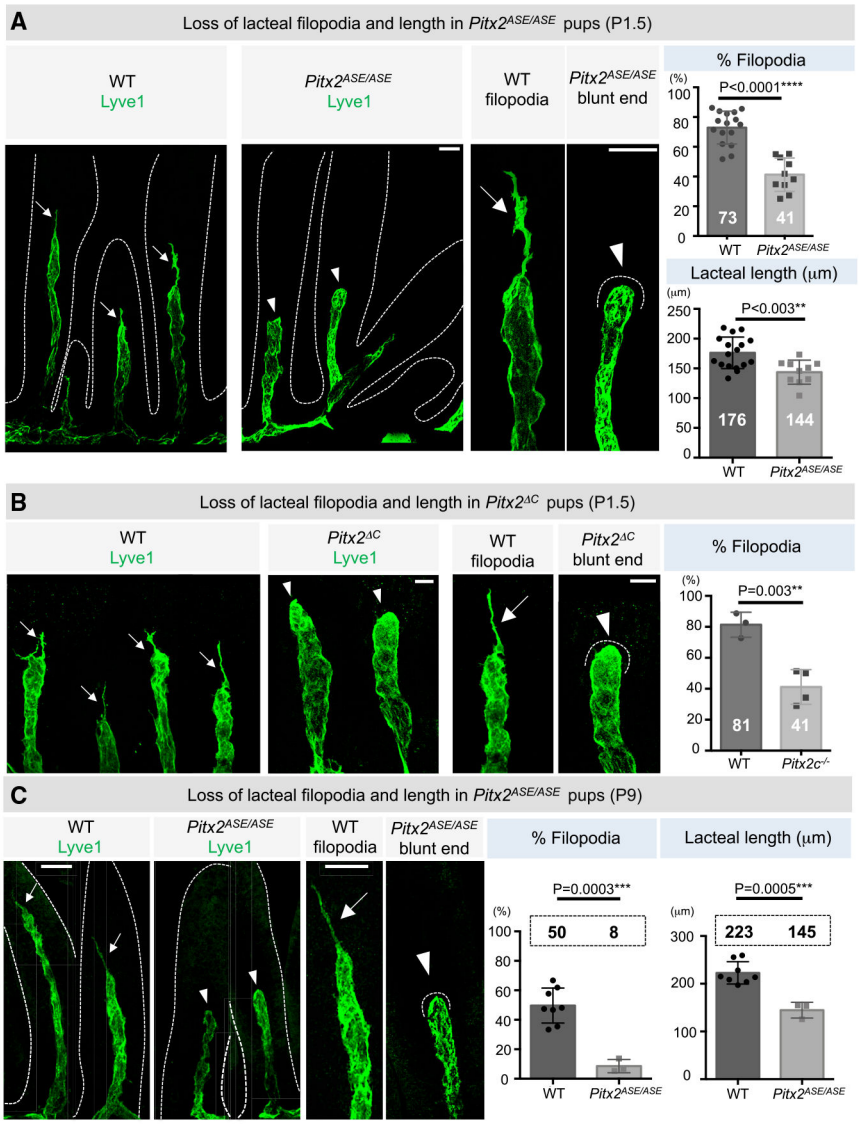

Figure 2. Shortened lacteals with missing filopodia in *Pitx2*$^{ASE/ASE}$ mice

(A) Whole-mount lacteals (Lyve-1, green) of WT and *Pitx2*$^{ASE/ASE}$ villi at P1.5. Top right: percent lacteals with filopodia. Bottom right: average lacteal length. Data are represented as mean ± SEM. P1.5 WT lacteals with filopodia = 72.90% ± 2.760%, n = 16; P1.5 *Pitx2*$^{ASE/ASE}$ lacteals with filopodia = 41.28% ± 3.545%, n = 10. Difference between WT and *Pitx2*$^{ASE/ASE}$ = −31.62% ± 4.476%. ****p < 0.0001. P1.5 WT lacteal length = 176.1 ± 6.401 μm, n = 17; P1.5 *Pitx2*^{ASE} lacteal length = 143.7 ± 6.392 μm, n = 10. Difference between WT and *Pitx2*$^{ASE/ASE}$ = −32.41 ± 9.704 μm. **p = 0.0026. White characters mark the mean in each group. Scale bars, 30 μm.

(B) Whole-mount lacteals (Lyve-1, green) of WT and *Pitx2*$^{\Delta C}$ villi at P1.5. Right: percent lacteals with filopodia. Data are represented as mean ± SEM. WT = 81.38% ± 4.660%, n = 3; *Pitx2*$^{\Delta C}$ = 41.13% ± 5.604%, n = 4; difference between WT and *Pitx2*$^{\Delta C}$ = −40.25% ± 7.692%; **p = 0.0034. White characters mark the mean in each group. Scale bar, 20 μm.

(C) Whole mount lacteals (Lyve-1, green) of WT and *Pitx2*$^{ASE/ASE}$ villi at P9. Left: percent lacteals with filopodia. Right: average lacteal length. Note the extended filopodium in WT lacteal tips (white arrows) versus the blunt-ended lacteals (white arrowhead) in ASE. Data are represented as mean ± SEM. P9 WT lacteals with filopodia = 49.66% ± 4.200%, n = 8; P9 *Pitx2*$^{ASE/ASE}$ lacteals with filopodia = 8.543% ± 2.610%, n = 3. Difference between WT and *Pitx2*$^{ASE/ASE}$ = −41.12% ± 7.237%. ***p = 0.0003. P9 WT lacteal length = 222.7 ± 8.252 μm, n = 8; P9 *Pitx2*$^{ASE/ASE}$ lacteal length = 144.6 ± 9.518 μm, n = 3. Difference between WT and *Pitx2*$^{ASE/ASE}$ = −78.12 ± 14.90 μm. ***p = 0.0005. Black characters mark the mean in each group. Scale bars, 30 μm.

See also Figure S2.

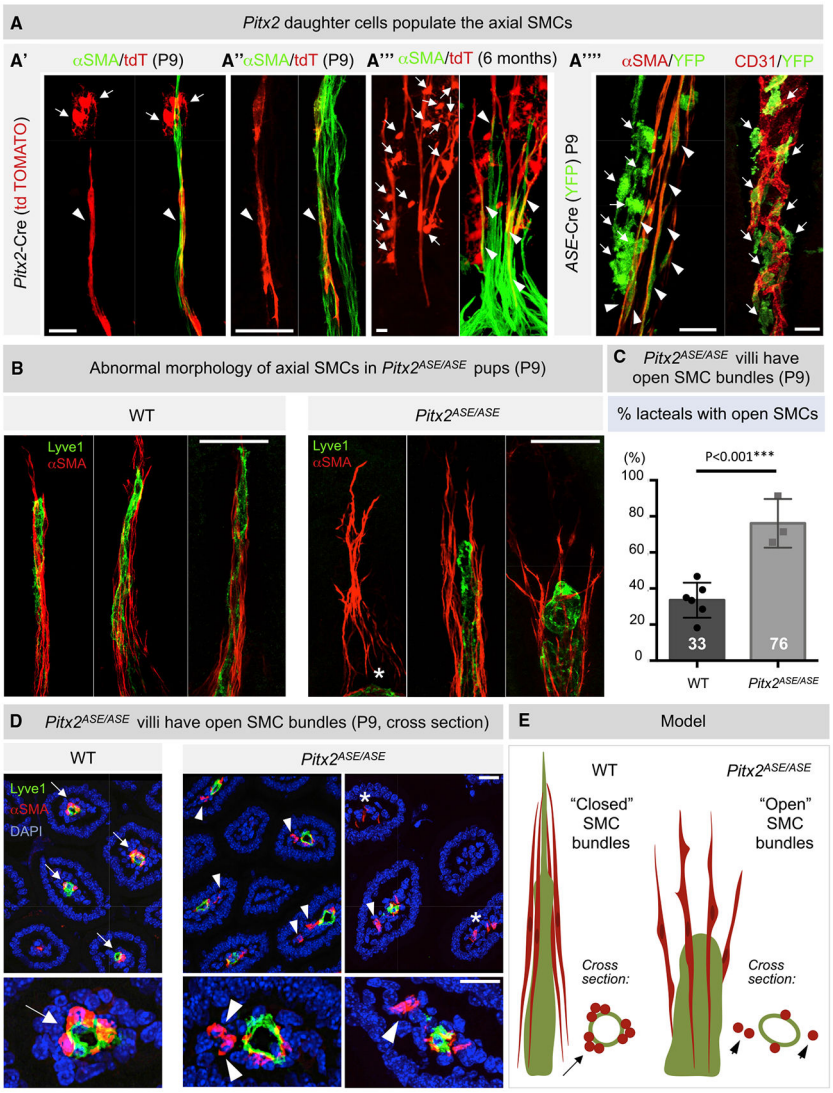

Figure 3. Malformation of the muscular-lacteal complex in *Pitx2*$^{ASE/ASE}$ mice

(A) Lineage tracing with *Pitx2*^{cre} - *ROSA26*$^{CAG\text{-}tdTomato}$ and *ASE*^{cre} - *ROSA26*$^{CAG\text{-}EYFP}$ mice; whole-mount villus from Pitx2^{cre};*ROSA26*$^{CAG\text{-}tdTomato}$ mice at P9 (A' and A") and 6 months (A"'). Note the colocalization of αSMA (green) and tdTomato (tdT, red) that marks axial SMCs of *Pitx2* descent (white arrowhead) and axial SMC heterogeneity (A"). White arrows indicate additional cell types marked by *Pitx2* daughters (A'). (A"") Whole mount villus from *ASE*^{cre} - *ROSA26*$^{CAG\text{-}EYFP}$ mice at P9. Note the colocalization of αSMA (red) and YFP (green) that marks axial SMCs of *ASE* descent (white arrowheads). White arrows indicate additional cell types marked by *ASE* daughters, distinct from BECs (red). Scale bar, 20 μm.

(B) Whole-mount muscular-lacteal complexes of WT and ASE at P9. Green is lacteal (Lyve-1); red is αSMA (smooth muscle). From left to right in the *Pitx2*$^{ASE/ASE}$ panel: aberrant muscular arrangement with no lacteal (white asterisk), loss of contact between axial SMCs and lacteal, and open axial SMCs with shorter and dilated lacteal. Scale bar, 40 μm.

(C) Percent lacteals surrounded by “open” axial SMCs based on data represented in (B). We defined the muscles as “open” when they were divergently aligned around the lacteal tip. Data are represented as mean ± SEM. P9 WT = 33.51% ± 3.950%, n = 6; P9 *Pitx2*$^{ASE/ASE}$ = 76.12% ± 7.775%, n = 3. Difference between WT and *Pitx2*$^{ASE/ASE}$ = 42.61% ± 7.703%, p = 0.0009***. White characters mark the mean in each group.

(D) Muscular-lacteal complexes at P9 in transverse sections. Green is lacteal (Lyve-1); red is αSMA (smooth muscle); blue is DAPI. Note the close (white arrows) versus distanced (white arrowheads) proximity of red and green signals. White stars mark villi with missing lacteals. Scale bar, 20 μm.

(E) Cartoon demonstrating muscular-lacteal arrangement of WT and *Pitx2*$^{ASE/ASE}$ mice. Green is lacteal; red is muscle. See also Figure S3.

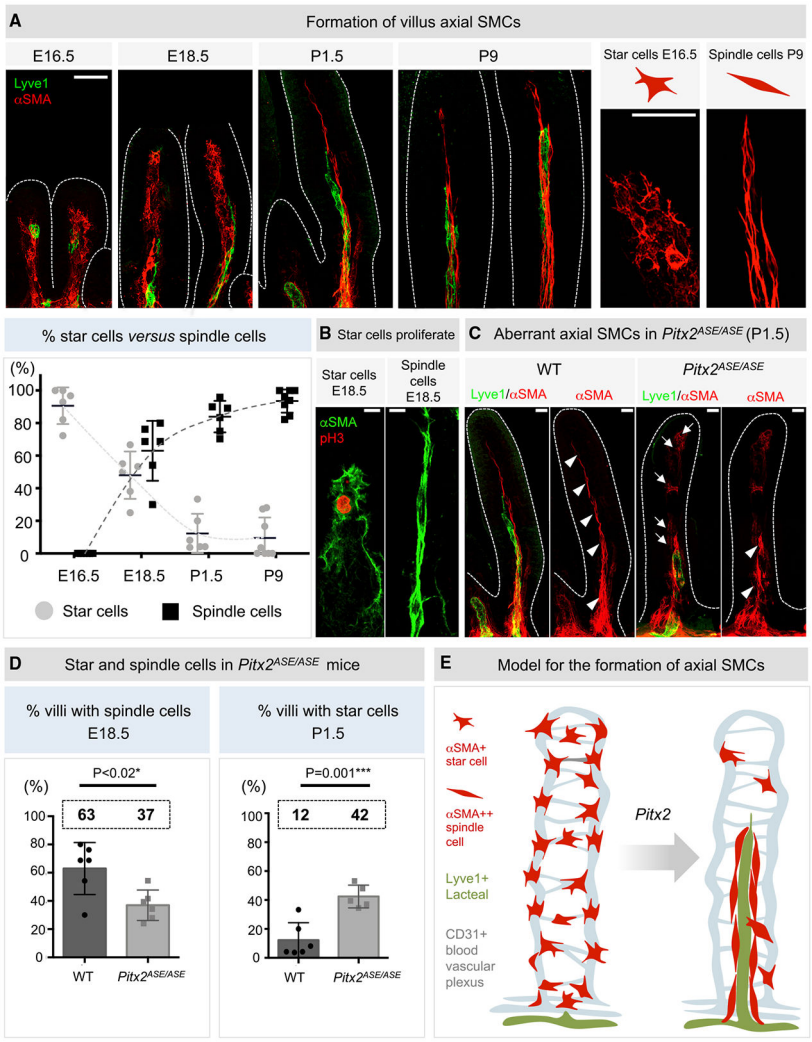

Figure 4. Lacteal-associated axial SMCs arise by *ASE*-dependent remodeling

(A) Whole-mount WT villous muscular-lacteal development from E16.5–P9. Green is lacteal (Lyve-1); red is αSMA (smooth muscle). Insets: note the shape difference of cells at E16.5 (star) versus at P9 (spindle). Scale bar, 40 μm. Graph: percent villi with αSMA^{+} star cells (black squares) or αSMA^{++} spindle cells (gray dots). Note the negative correlation between αSMA^{+} star cells (dominant in prenatal stages) and αSMA^{++} spindle cells (dominant postnatally). Data displayed on the y axis are represented as mean ± SEM. E16.5 villi with star cells = 90.7% ± 4.6%, n = 6; E16.5 villi with bundles = 0% ± 0%, n = 6; E18.5 villi with star cells = 48.02% ± 5.9%, n = 6; E18.5 villi with muscle bundles = 62.98% ± 7.5%, n = 6; P1.5 villi with star cells = 12.25% ± 4.9%, n = 6; P1.5 villi with muscle bundles = 83.95% ± 4.0%, n = 6; P9 villi with star cells = 9.454% ± 4.5%, n = 8; P9 villi with muscle bundles = 93.51% ± 2.5%, n = 8.

(B) Star but not spindle cells are proliferative (E18.5). Whole-mount WT villus; green is αSMA (green), red is phospho-histone 3 (pH3), and blue is DAPI. Note that the pH3 signal colocalized only with star- but not spindle-like SMCs. Scale bar, 10 μm.

(C) Whole-mount muscular-lacteal complexes from WT and ASE siblings at P9. Green is lacteal (Lyve-1); red is αSMA (smooth muscle). Note the retention of SMA^{+} star cells in $Pitx2^{ASE/ASE}$. Scale bar, 20 μm.

(D) Percent villi with star or spindle cells in WT and ASE siblings. Left: percent villi with spindle cells in E18.5 embryos. Right: percent villi with star cells in P1.5 pups. Data displayed on y axes are represented as mean ± SEM. E18.5 WT villi with spindles = 62.98% ± 7.52%, n = 6; E18.5 $Pitx2^{ASE/ASE}$ villi with spindles = 36.93% ± 4.41%, n = 6. Difference between WT and $Pitx2^{ASE/ASE}$ = −26.05% ± 8.72%, *p = 0.0136. P1.5 WT villi with stars = 12.25% ± 4.917%, n = 6; P1.5 $Pitx2^{ASE}$ villi with stars = 42.42% ± 3.510%, n = 5. Difference between WT and $Pitx2^{ASE/ASE}$ = 30.18% ± 6.292%, ***p = 0.0010.

(E) Cartoon depicting star-to-spindle smooth muscle transition to form the axial SMC-lacteal complex.

See also Figure S4.

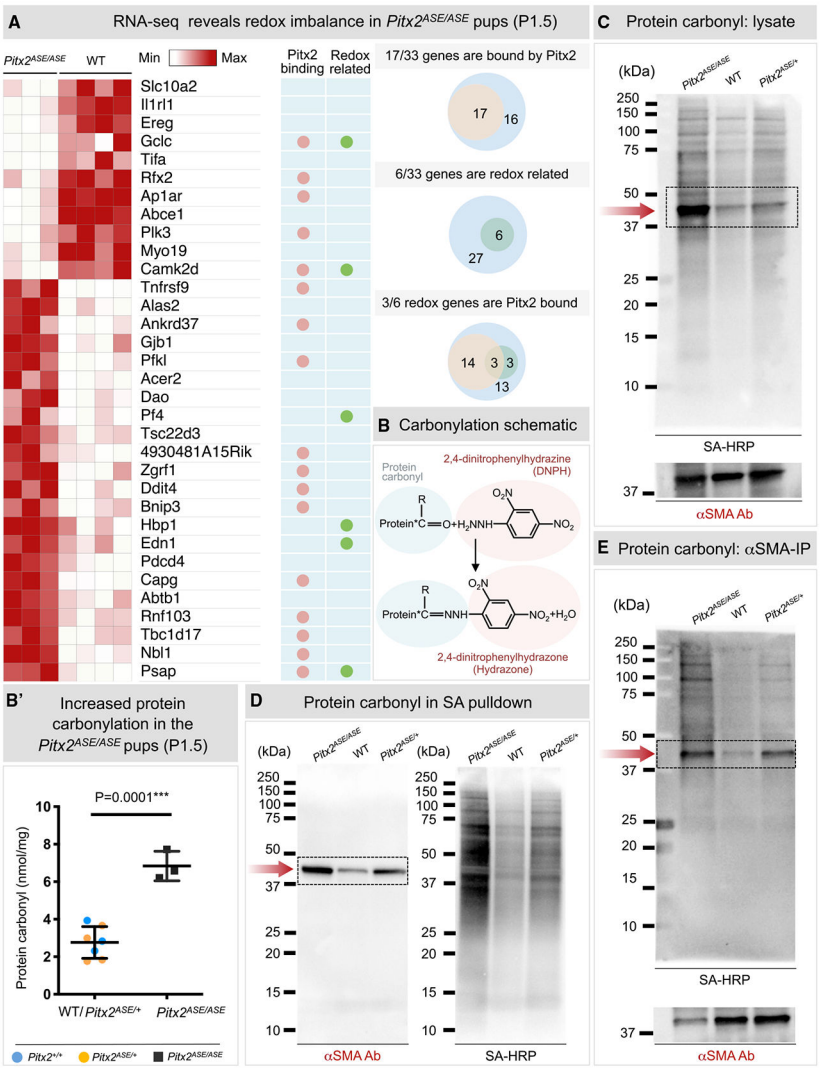

Figure 5. *ASE* deletion leads to redox imbalance and actin carbonylation in intestinal smooth muscle

(A) RNA-seq. Left: heatmap of differentially expressed genes at P1.5. The relative minimum expression is depicted in white and maximum in red. Red dots show genes bound by Pitx2 based on prior chromatin immunoprecipitation sequencing (ChIP-seq); green dots show genes with known ROS function. Right: Venn diagrams of differentially expressed genes bound by *Pitx2* and/or with reported function in redox balance.

(B) 2,4-dinitrophenylhydrazine (DNPH, or HZ) reacts with protein carbonyl groups, forming stable 2,4-dinitrophenylhydrazone (hydrazone), quantified spectrophotometrically (B'). Protein carbonyl concentration measured from WT (blue), $Pitx2^{ASE/+}$ (orange), and $Pitx2^{ASE/ASE}$ (black) intestines. Data are represented as mean ± SEM. Protein carbonyl in the WT/$Pitx2^{ASE/+}$ group = 2.76 ± 0.3194 nmol/mg, n = 7; protein carbonyl in $Pitx2^{ASE/ASE}$ = 6.833 ± 0.4567 nmol/mg, n = 3. Difference between WT/Het and $Pitx2^{ASE/ASE}$ = 4.073 ± 0.5741 nmol/mg, ***p = 0.0001.

(C–E) P1.5 gut protein lysates labeled with biotin-HZ, separated by SDS-PAGE, then transferred to a nitrocellulose membrane.

(C) Total protein carbonyl detected by streptavidin-HRP (SA-HRP) (top blot) and total αSMA expression by αSMA antibody on the same blot (bottom blot).
(D) Left: αSMA detected by an αSMA antibody. Right: total protein carbonyl detected by SA-HRP on the same blot.
(E) P1.5 gut protein extracts were labeled with biotin-HZ following αSMA immunoprecipitation (SMA-IP), separated by SDS-PAGE, then transferred to a nitrocellulose membrane. Total protein carbonyl was detected by SA-HRP (top blot). SMA-IP efficiency was confirmed by total αSMA expression, detected by αSMA antibody on the same blot.
See also Figure S5.

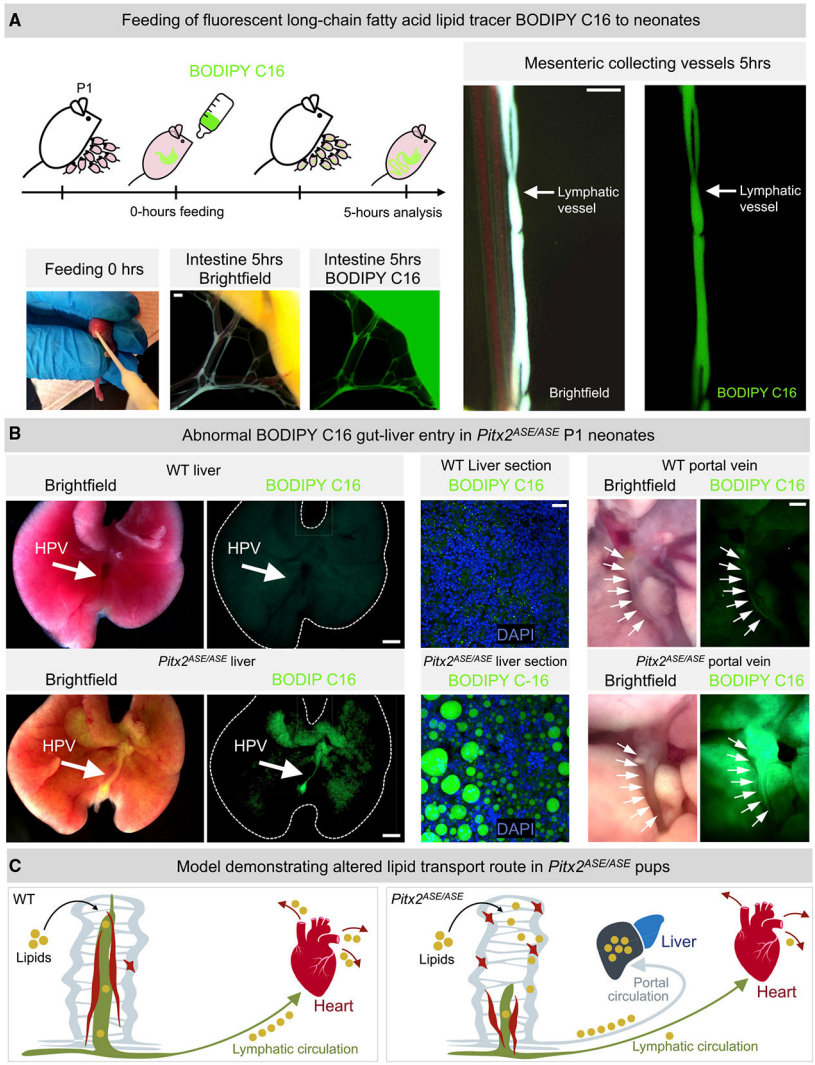

Figure 6. *ASE* is required for the normal route of dietary lipid transport

(A) Pups were fed with BODIPY FL C16 and then left with the dam for 5 h before analyses. Note entry of the tracer in mesenteric collectors in the WT validating feeding assay. Scale bar, 200 μm.

(B) Hepatic analysis of tracer accumulation in *Pitx2*$^{ASE/ASE}$ at P1. Left to right: analysis of whole livers, frozen liver sections with DAPI counterstain (blue), and hepatic portal vein (HPV; white arrows) in WT (top) and *Pitx2*$^{ASE/ASE}$ (bottom) neonates. Note the enriched green signal in HPVs and livers of *Pitx2*$^{ASE/ASE}$ neonates in comparison with the WT. Scale bars: 1 mm (left, liver, whole organ), 20 μm (center, liver section), and 300 μm (right, HPV).

(C) Lymphatic system-dependent transport (green) of dietary fats (yellow dots) is dominant in WT mice, whereas additional activation of lymphatic system-independent fat transport via the HPV (light blue) is evident in ASE mice. Red marks star and axial SMCs.

See also Figures S6, S8, and S9.

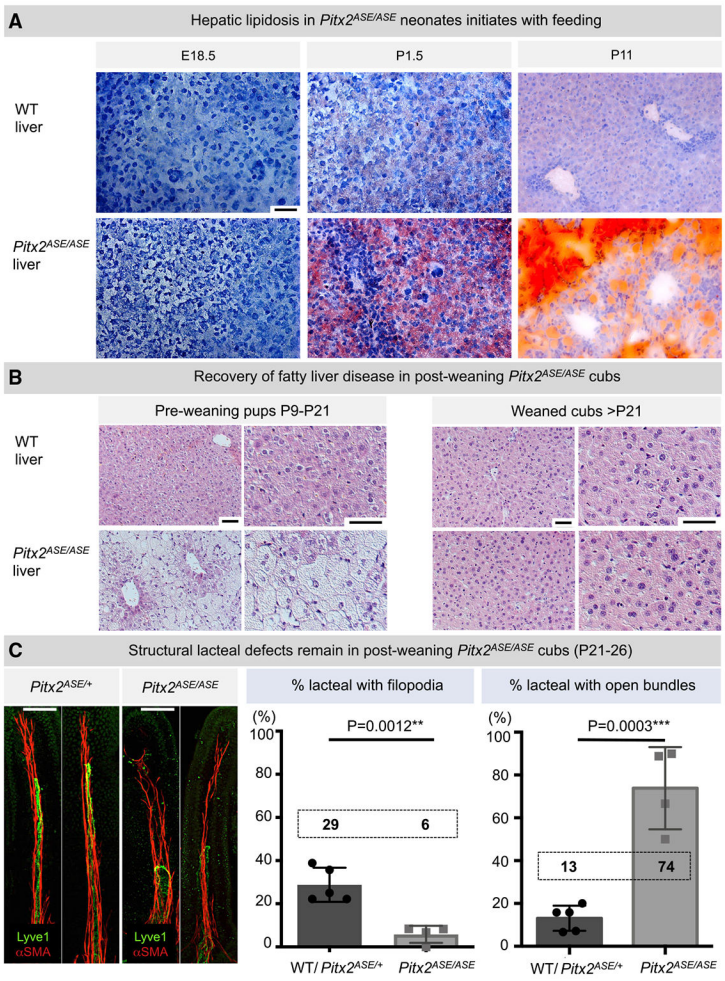

Figure 7. *Pitx2*$^{ASE/ASE}$ mice develop diet-induced fatty liver

(A) Hematoxylin (blue) and oil red O (red) staining of liver sections from E18.5, P1.5, and P11 WT (top) and *Pitx2*$^{ASE/ASE}$ mice (bottom). Scale bar, 50 μm.

(B) Histology of WT (top) and *Pitx2*$^{ASE/ASE}$ (bottom) livers isolated from suckling pups (left) and weanlings (right). Note lipid vacuoles and loss of eosinophilic parenchymal stain in *Pitx2*$^{ASE/ASE}$ pups, resolved in *Pitx2*$^{ASE/ASE}$ weanlings. Images shown on the right are high magnifications of the left adjacent image. Scale bar, 50 μm.

(C) Structural muscular-lacteal defects remain in post-weaning *Pitx2*$^{ASE/ASE}$ cubs. Left: whole-mount muscular-lacteal complexes from WT and ASE cubs at P26. Note shorter lacteals (Lyve-1, green) and a more open muscular arrangement (αSMA, red) in ASE but not WT weanlings. Right: quantification of percent lacteals with filopodia and open muscle bundles. Note that the following mice were pooled: n = 4 WT at P21 with n = 1 *Pitx2*$^{ASE/+}$ at P26; the *Pitx2*$^{ASE/ASE}$ group consisted of n = 3 at P21 and n = 1 at P26. Data displayed on y axes are represented as mean ± SEM. Lacteals with filopodia in WT weanlings = 28.81% ± 7.915%, n = 5; lacteals with filopodia in *Pitx2*$^{ASE/ASE}$ weanlings = 5.833% ± 3.967%, n = 4. Difference between WT and *Pitx2*$^{ASE/ASE}$ = −22.98% ± 4.375%; **p = 0.0012. Lacteals with open muscle bundles in WT weanlings = 13.08% ± 2.637%, n = 5; lacteals with open bundles in *Pitx2*$^{ASE/ASE}$ weanlings = 73.85% ± 9.599%, n = 4. Difference between WT and

Pitx2$^{ASE/ASE}$ = 60.77% ± 8.945%; ***p = 0.0003. Black characters represent the mean of each group. Scale bar, 50 μm.

See also Figure S7.

KEY RESOURCES TABLE

REAGENT or RESOURCE	SOURCE	IDENTIFIER
Antibodies		
Rabbit polyclonal Lyve-1 antibody	Abcam	ab14917; RRID:AB_301509
CD31 Rat anti-Mouse	BD Sciences	553370; RRID:AB_394816
Rabbit anti-Myosin, Smooth Muscle Heavy Chain	Alfa Aesar	BT-563
Anti-Actin, α-Smooth Muscle	Sigma	A2547; RRID:AB_476701
Anti-Actin, α-Smooth Muscle-FITC	Sigma	F3777; RRID:AB_476977
Anti-Actin, α-Smooth Muscle - Cy3	Sigma	C6198; RRID:AB_476856
Anti-Histone H3 antibody	Abcam	Ab5176; RRID:AB_304763
Rabbit Anti-Mouse IgG H&L (HRP)	Abcam	ab6728; RRID:AB_955440
Alexa Fluor 488 goat anti-rabbit IgG (H+L)	Fisher	A11070; RRID:AB_2534114
Donkey polyclonal Secondary Antibody to Rabbit IgG - H&L (Alexa Fluor® 647)	Abcam	ab150075; RRID:AB_2752244
Goat anti-Rat IgG (H+L) Cross-Adsorbed, Alexa Fluor 488	Fisher	A11006; RRID:AB_2534074
Goat polyclonal Secondary Antibody to Rat IgG - H&L (Alexa Fluor® 594)	Abcam	ab150160; RRID:AB_2756445
Goat anti-rabbit antibody Alexa Fluor 568	Thermo Fisher	A-11011; RRID:AB_143157
Donkey polyclonal Secondary Antibody to Rat IgG - H&L (Alexa Fluor® 647)	Abcam	ab150155; RRID:AB_2813835
Chemicals, peptides, and recombinant proteins		
Dapi	ThermoFisher	D1306
Prolong Gold antifade reagent 10mL without DAPI	Invitrogen	P36930
FocusClear	Celexplorer	FC-101
EZ-Link Hydrazide-Biotin	Thermo Scientific	21339
Peroxidase Streptavidin	Jackson Immuno	016030084
Pierce High Capacity Streptavidin Agarose	Thermo Scientific	20357
Protein G Sepharose beads	Abcam	ab193259
Western Lightning Plus-ECL	PerkinElmer Inc.	NEL104001EA
BODIPY FL C16	ThermoFisher	D3821
Oil red O	Abcam	ab150678
MOWIOL® 4-88 Reagent, Gelvatol	EMD Millipore	EM475904
Hematoxylin (Modified Mayer's)	Abcam	Ab220365
Halt Protease and Phosphatase Inhibitor Cocktail	Thermo	78336
Pierce DTT (Dithiothreitol), No-Weigh Format	Thermo	A39255
Intralipid	Sigma	I141
Glutaraldehyde 25% in aqueous solution, EM grade	Electron Microscopy Sciences	16220
16% Paraformaldehyde (formaldehyde) aqueous solution	Electron Microscopy Sciences	15710
Sorensen's Phosphate Buffer, 0.2M, pH 7.2	Electron Microscopy Sciences	11600-10
Critical commercial assays		
Protein Carbonyl Colorimetric Assay Kit	Cayman	75816-674
In Situ Cell Death Detection Kit, TMR red	Sigma	45-12156792910
PAXgene Tissue FIX	QIAGEN	765312, 765512

REAGENT or RESOURCE	SOURCE	IDENTIFIER
Deposited data		
P1.5 Whole gut ASE RNaseq	Cornell University	GSE160677
Experimental models: Organisms/strains		
Pitx2^{ASE}	Osaka University	N/A
Pitx2$^{\Delta C}$	Baylor College of Medicine	N/A
Pitx2^{cre}	Baylor College of Medicine	N/A
ASE^{cre} (referred to as "Pitx2^{Cre}" in Shiratori et al., 2006)	Riken	N/A
ROSA26$^{CAG\text{-}tdTomato}$	Jacksons lab	Jax 007905
ROSA26-EYFP	Jacksons lab	Jax 006148
Oligonucleotides		
Primers for mouse genotyping	See Table S1	N/A
Software and algorithms		
FIJI	National Institutes of Health	https://fiji.sc/; RRID: SCR_002285
Prism 8	GraphPad	http://www.graphpad.com/; RRID: SCR_002798
Imaris 9.5	Bitplane	https://imaris.oxinst.com/; RRID:SCR_007370
ZEN	Zeiss	https://www.zeiss.com/microscopy/us/products/microscope-software/zen.html#introduction; RRID:SCR_013672